NASA/TM–2011-217171

Statistical Energy Analysis (SEA) and Energy Finite Element Analysis (EFEA) Predictions for a Floor-Equipped Composite Cylinder

Ferdinand W. Grosveld
Lockheed Martin, Hampton, Virginia

Noah H. Schiller and Randolph H. Cabell
Langley Research Center, Hampton, Virginia

August 2011

NASA STI Program . . . in Profile

Since its founding, NASA has been dedicated to the advancement of aeronautics and space science. The NASA scientific and technical information (STI) program plays a key part in helping NASA maintain this important role.

The NASA STI program operates under the auspices of the Agency Chief Information Officer. It collects, organizes, provides for archiving, and disseminates NASA's STI. The NASA STI program provides access to the NASA Aeronautics and Space Database and its public interface, the NASA Technical Report Server, thus providing one of the largest collections of aeronautical and space science STI in the world. Results are published in both non-NASA channels and by NASA in the NASA STI Report Series, which includes the following report types:

- TECHNICAL PUBLICATION. Reports of completed research or a major significant phase of research that present the results of NASA programs and include extensive data or theoretical analysis. Includes compilations of significant scientific and technical data and information deemed to be of continuing reference value. NASA counterpart of peer-reviewed formal professional papers, but having less stringent limitations on manuscript length and extent of graphic presentations.

- TECHNICAL MEMORANDUM. Scientific and technical findings that are preliminary or of specialized interest, e.g., quick release reports, working papers, and bibliographies that contain minimal annotation. Does not contain extensive analysis.

- CONTRACTOR REPORT. Scientific and technical findings by NASA-sponsored contractors and grantees.

- CONFERENCE PUBLICATION. Collected papers from scientific and technical conferences, symposia, seminars, or other meetings sponsored or co-sponsored by NASA.

- SPECIAL PUBLICATION. Scientific, technical, or historical information from NASA programs, projects, and missions, often concerned with subjects having substantial public interest.

- TECHNICAL TRANSLATION. English-language translations of foreign scientific and technical material pertinent to NASA's mission.

Specialized services also include creating custom thesauri, building customized databases, and organizing and publishing research results.

For more information about the NASA STI program, see the following:

- Access the NASA STI program home page at *http://www.sti.nasa.gov*

- E-mail your question via the Internet to help@sti.nasa.gov

- Fax your question to the NASA STI Help Desk at 443-757-5803

- Phone the NASA STI Help Desk at 443-757-5802

- Write to:
  NASA STI Help Desk
  NASA Center for AeroSpace Information
  7115 Standard Drive
  Hanover, MD 21076-1320

NASA/TM–2011-217171

Statistical Energy Analysis (SEA) and Energy Finite Element Analysis (EFEA) Predictions for a Floor-Equipped Composite Cylinder

Ferdinand W. Grosveld
Lockheed Martin, Hampton, Virginia

Noah H. Schiller and Randolph H. Cabell
Langley Research Center, Hampton, Virginia

National Aeronautics and
Space Administration

Langley Research Center
Hampton, Virginia 23681-2199

August 2011

Available from:

NASA Center for AeroSpace Information
7115 Standard Drive
Hanover, MD 21076-1320
443-757-5802

TABLE OF CONTENTS

LIST OF TABLES

LIST OF FIGURES

INTRODUCTION

Finite Element Analysis (FEA), Boundary Element Analysis (BEA) and Statistical Energy Analysis (SEA) have been used for several decades to analyze vibro-acoustic problems and have matured to the point that reliable predictions can be expected cognizant of the limitations of each method. These prediction tools have been validated for numerous structurally and/or acoustically excited aerospace, automotive, shipbuilding, and architectural structures in anechoic, reverberant and in-situ acoustic environments. It is generally accepted that the discrete FEA and BEA numerical analyses are applicable towards the low end of the frequency scale, where the individual modal response is dominant. SEA is applied at frequencies where the modal density and the modal overlap are high. Predictions of the vibro-acoustic response made by the FEA and SEA analysis tools were compared with structural and acoustic measurements on a floor-equipped, composite cylinder in the 1980s (References 1-6). This composite test cylinder was originally developed to resemble a composite aircraft fuselage for impact dynamics and acoustic transmission verification (Reference 7). In the last few decades new measurement equipment, improved experimental tools, and increased data storage have become available to enhance the experimental characterization of a structure such as the composite cylinder. Innovative hybrid analysis and prediction tools have emerged to take advantage of both finite element modeling and statistical analysis. A new set of measurements and predictions of the vibro-acoustic response of the composite cylinder is being pursued to validate these new analysis tools and enhance the physical understanding of the problem.

Comet Enflow developed by the Comet Technology Corporation is a commercially available, high frequency vibroacoustic analysis software founded on Energy Finite Element Analysis (EFEA) and Energy Boundary Element Analysis (EBEA). The EFEA is based on deriving governing differential equations in terms of energy density variables and then employing a finite element approach to numerically solve them. In the EFEA, both the structural and acoustic domains are modeled using finite elements. Joint elements based on power flow continuity across the junction are utilized at the interface of geometric and material discontinuities. In this method the same FEA mesh developed for structural and acoustic low frequency analyses can be used for the high frequency solutions. In a program managed by the NASA Langley Research Center Structural Acoustics Branch, EFEA as implemented in Comet Enflow 2009 is being validated on the floor-equipped composite cylinder by comparing EFEA vibroacoustic response predictions with SEA and experimental results. The SEA predictions are made using the commercial software program VA One 2009 from ESI Group. Comet Enflow predicted response for the power flow from an acoustic space to a structural subsystem was investigated in Reference 8. The purpose of the current study is to compare VA One and Comet Enflow predictions for the floor-equipped composite cylinder with respect to the root-mean-square velocity of the shell and the sound pressure levels in the cavity above the floor. The predictions will be compared with experimental results in a future effort. The frequency region of interest for this study covers the one-third octave bands with center frequencies from 100 Hz to 4000 Hz.

COMPOSITE CYLINDER CONFIGURATION

The composite cylinder test article (Figure 1) is a 3.658 m long filament-wound, stiffened cylinder with a 1.676 m diameter. The composite material of the cylinder shell consists of carbon fibers embedded in an epoxy resin. The nine-layer ply-sequence of the cylinder shell is $\pm 45, \pm 32, 90, \mp 32, \mp 45$ for a total thickness of 1.7019 mm. The cylinder is stiffened by ten evenly spaced J-section ring frames and twenty-two evenly spaced hat-section longitudinal stringers. A 12.7 mm thick plywood floor is installed 0.544 m above the bottom of the cylinder. The floor is carried by ten horizontal aluminum beams at the locations of the ring frames. Twenty vertical aluminum beams support the floor, with one pair of supporting beams

in each ring frame cross-section and spaced 1.045 m apart. The shell and stiffener elements of the fuselage model are rivet-bonded together. Figure 2 depicts a cross-section of the cylinder showing the beam supported floor, a ring frame and the cross-sections of the twenty longitudinal stringers. A support structure consisting of two rigid 0.0889 thick medium-density fiberboard (MDF) endcaps provide constrained edge conditions to the cylinder. The cylinder rests in grooves carved out in the endcaps and the entire structure is held together by four tension rods. Wooden beams are attached to each tension rod to increase damping. A hinged door (0.61 m by 0.61 m) was incorporated in the front endcap to provide access to the interior of the cylinder. The access door can be locked into place by six over-center latches as shown in Figure 1.

NUMERICAL MODELS OF THE COMPOSITE CYLINDER

Finite Element Model

A finite element model of the floor-equipped composite cylinder was developed using the pre/post-processor MSC.Patran 2007 Rev.2. The model development including the geometry, the element property sets, the composite material lay-up, the mechanical material properties, the beam section properties and other characteristics of the model is presented in Reference 9. A wireframe isometric view of the composite cylinder finite element model is presented in Figure 3 without the front endcap to more clearly show the floor and the supporting beams. The model consists of a total 2242 CQUAD4 plate elements for the cylinder shell, the floor and the two endcaps. The longitudinal stringers, the ring frames, the floor beams and the floor supports were modeled using 1198 CBEAM beam elements. The two acoustic cavities above and below the floor consist of 5452 CHEXA three-dimensional elements. The volume, bounding area and total perimeter values of the acoustic cavities above and under the floor are presented in Table 1.

The mechanical properties of the shell, the ring frames, the longitudinal stringers, the floor, the floor support beams and the endcaps are listed in Table 2 and include the elasticity moduli, the shear modulus, the density and the Poisson ratios. The beam section properties are listed in Table 3 including the cross-sectional area, the moments of inertia, the torsional constant about the centroid, and the shear stiffness factors. The cross-sectional dimensions of the ring frames and the longitudinal stiffeners supporting the cylinder shell were measured in situ yielding slightly different values for the beam section properties in Table 3 than reported in Reference 9, which were obtained from the composite cylinder design report[7].

Statistical Energy Analysis Model

The SEA model depicted in Figure 4 was constructed by importing the geometry and the nodes of the floor-equipped composite cylinder finite element model into the VA One prediction program. The bays bounded by the ring frames and the longitudinal stringers were modeled as subsystems consisting of singly curved shells having a thickness of 1.7 mm and a radius of 0.8382 m. The smaller bays above the floor were also modeled using singly curved shells. These bays were bounded by the floor, two ring frames and a stringer. The bays adjacent to, but below the floor, were represented by flat plates since these bays were small and not enough nodes were available from the finite element model to define the curvature of those subsystems. The composite nine-layer shell was represented by the equivalent orthotropic material properties of the finite element model (Table 2). The 0-degree fiber orientation was defined parallel to the cylinder axis. The composite ring frames and longitudinal stringers were modeled with isotropic material properties as this was the only option available for beam sections in VA One 2009. The isotropic material properties for the beam subsystems are listed in Table 4. The beam section properties including the shear center offsets were taken from the finite element model listed in Table 3.

The horizontal floor beams and the vertical beams supporting the floor were modeled using aluminum with section properties derived from the finite element model (Table 3). The plywood floor and the two MDF endcaps were represented by flat plate subsystems with finite element model derived mechanical material properties (Table 2). The subsystems for the acoustic cavities above and below the floor were defined by the geometry of the cylinder finite element model and the volume, area and perimeter parameters listed in Table 1. The properties of the air included a mass density of 1.21 kg/m^3 and a speed of sound of 343 m/s.

The flexural damping loss factors of the cylinder shell and floor, and the damping loss factors of the acoustic cavity subsystems were estimated experimentally using the impulse response decay method (IRDM)[10,11,12] and the interrupted noise method, respectively. However since the flexural loss factors for the shell and floor were estimated in-situ, the estimates are anticipated to be high since they account for losses due to damping as well as coupling. The damping loss factors are tabulated in Table 5. The extensional and shear damping loss factors of the shell and the floor, and all the damping loss factors of the beams and the endcaps were arbitrarily chosen to equal 0.01 and were included in the SEA matrix solution.

Junctions between subsystems were automatically created using the autoconnect feature in VA One resulting in 332 point, 568 line, and 279 area junctions. The junctions are shown in Figure 5. The front area junctions between the upper acoustic cavity and the front endcap, and between the lower acoustic cavity and the endcap were removed for clarity. Only resonance energy paths were considered.

Energy Finite Element Analysis Model

The finite element bulk data file including the geometry, element properties and material properties was imported into Comet Enflow. The program automatically generates junctions at geometric and material discontinuities resulting in 324 point joints, 1272 line joints and 2048 area joints. The 324 beam-beam point joints are shown in Figure 6a. The line joints consist of 174 plate-plate joints and 1198 plate-beam-plate line joints which are depicted in Figure 6b. The 1700 plate-acoustic joints and the 348 plate-acoustic-plate joints are shown in Figure 6c. The number of EFEA point joints is about the same as the number of SEA point junctions. However, the number of EFEA line and area joints is much larger than the number of SEA line and area junctions as the automatic joint generation in EFEA is based on the finite elements while the SEA modeling is based on shell subsystems bounded by the ring frames and longitudinal stringers. This is illustrated in Figure 5 where a SEA shell subsystem is bounded by four stiffener segments and is represented by one area junction and four line junctions, compared to the same cylinder shell area in EFEA which consists of six area joints (Figure 6c) and ten line joints (Figure 6b). Similarly, the number of EFEA plate-acoustic-plate joints is much higher than the SEA area junctions for the cylinder floor. The increased size of the energy balance matrix will increase the computation time to obtain a solution for the matrix. The radiation dimensions of the single bay radiating subsystem were specified in the input data file along with a curvature of 1.193 for the cylinder shell. The same beam section properties were input for the beam stiffeners as were used to define the SEA beam elements. In addition, the St. Venant's ratio was defined as the square-root of the ratio of the torsion constant and the polar moment of inertia, which was equal to 0.049 for the ring frame, 0.0858 for the longitudinal stiffeners and 0.0543 for the floor beams and floor supports. The volume, area and perimeter parameters of the cavity above and below the floor (Table 1) were entered into the Comet Enflow data file. The same damping loss factors as in the SEA formulation (Table 5) were used for the shell, the floor, the stiffeners, the endcaps, and the acoustic cavities. Only resonance energy paths were considered. Comet Enflow was executed using the default Gaussian Elimination solver.

COMPARISON BETWEEN SEA AND EFEA PREDICTIONS

The SEA model was excited by a unit power input at the location of Bay X, which is the shell subsystem bounded by two longitudinal stringers and two ring frames (Figure 7). The SEA predictions were performed with VA One following the recommendations of the User's Manual in Reference 13. Bay X in the EFEA model consists of six elements and two interior nodes not coinciding with the bay boundaries. The unit power input for the EFEA analysis was applied to the bay interior Node 1538 which is located closest to the back endcap. The Comet Enflow User's Manual[14] describes the program execution, the input and output file management and the input entries to the code for the EFEA predictions. The SEA and EFEA structural response levels of the cylinder shell and the sound pressure levels in the acoustic cavities were predicted by the VA One and Comet Enflow software programs and are compared in the following sections.

Structural Response Predictions

Structural response predictions were performed for Bay X and Bays 1-14 of the floor-equipped composite cylinder, the locations of which are indicated in Figure 7. This section compares predictions from the SEA and EFEA methods for two sidewall configurations and a complete model of the composite cylinder. The acoustic cavities below and above the floor were included in the structural analysis of the complete model, but their presence had a negligible effect on the structural response of the cylinder components. The input to the prediction codes, including mechanical material properties, geometrical characteristics and damping loss factors (Table 2 - Table 5), was the same for both energy methods to ensure an equitable comparison. Where possible, the energy paths and associated computational procedures in the two energy methods were also specified to match one another.

The first configuration discussed here consists of a portion of the sidewall only, with no stiffeners. The area of the sidewall structure covered the fifteen numbered bays of the cylinder (Figure 7) such that the total modeled section is the segment shown in Figure 8. The structure was represented in SEA by a singly-curved panel subsystem. A unit power excitation was applied to the subsystem and a single, spatially averaged root-mean-square velocity was predicted in VA One for the entire subsystem. The resulting velocity is shown in Figure 9 as a function of frequency. In EFEA, the sidewall was modeled using a relatively coarse finite element mesh which contained six plate elements per subpanel, for a total of ninety plate elements for the entire sidewall structure. A finite element approach is employed in Comet Enflow to solve the governing differential equation in terms of energy density variables numerically at the node locations of the model. This allows evaluating the root-mean-square velocity variations from node to node within the sidewall structure subsystem. The excitation corresponded to a unit power input at the location of one of the two nodes within the imaginary Bay X as indicated in Figure 8. For the results shown here, the nodal velocities were averaged over the nodes inside each imaginary bay, and the resulting root-mean-square velocities are shown in Figure 10 for the locations of the imaginary bays X and 5-8. Since there are no stringers and ring frames, the velocity response decays when moving away from the excitation location due to the structural damping of the sidewall material. The bay-to-bay response variation is more obvious when the velocity variation is plotted along a horizontal line parallel to the centerline of the sidewall, through the excitation point. This velocity variation for the Comet Enflow predictions is shown in Figure 11 for the 200 Hz one-third octave band and compared to the unvarying response of the VA One prediction. The EFEA prediction, shown at each node, decays exponentially away from the drive point due to damping in the sidewall. A similar comparison for the root-mean-square velocity predictions as function of nodal location is presented in Figure 12 for the 2000 Hz one-third octave band. Excellent agreement is observed between the SEA and EFEA energy methods when the Comet Enflow results are averaged over all nodes of the sidewall structure as evidenced in Figure 13.

The second configuration incorporated longitudinal stringers and ring frames, dividing the sidewall structure into fifteen individual bays as shown in Figure 14. The longitudinal stringers and ring frames were modeled as beam subsystems at the connecting lines between the bay subsystems. The autoconnect feature in VA One was used to create the point and line junctions connecting the bay subsystems. The SEA root-mean-square velocity predictions for Bay X and Bays 5-8 are shown in Figure 15 while the Comet Enflow results are presented in Figure 16. The results in the figures show a large discrepancy between the EFEA and SEA models at frequencies below 1000 Hz. After further study, it was determined Comet Enflow does not account for energy in the beams. To confirm this finding, the VA One SEA model was modified so the flexural, torsional, and extensional beam energies were excluded from the solution matrix. The resulting response predictions are shown in Figure 17 showing much better agreement with the EFEA results in Figure 16. These results appear to confirm that the Comet Enflow EFEA model does not consider beam energies in the solution.

More detailed comparisons on a bay-by-bay basis of the SEA (with no beam energy) and EFEA predictions are presented in Figure 18 through Figure 22. Within the driven Bay X, the higher VA One root-mean-square velocity predictions above 315 Hz (Figure 18) may be partially attributed to the different formulations defining the SEA coupling loss factor and the EFEA equivalent coupling loss factor. The average coupling loss factor η_{ij} for a line junction (Figure 5) between adjacent shell subsystems '*i*'and '*j*' is defined in SEA by[15]

$$\eta_{ij} = \frac{c_{gi} L}{\omega A_i} \frac{\tau_{ij}}{2 - \tau_{ij}} \tag{1}$$

where c_{gi} is the flexural group speed, τ_{ij} is the power transmission coefficient, ω is the rotational frequency, L is the length of the line junction, and A_i is the surface area of the subsystem. In EFEA the coupling loss factor of a conservative joint at a line discontinuity between two bay subsystems is analogous to the expression for the point coupling of two beams given in Reference 16

$$\eta_{ij} = \frac{c_{gi} L}{\omega A_i} \frac{\tau_{ij}}{r_{ii} + r_{jj}} \tag{2}$$

where the reflection coefficients r_{ii} and r_{jj} are defined by $r_{ii}=1-\tau_{ij}$ and $r_{jj}=1-\tau_{ji}$ resulting in

$$\eta_{ij} = \frac{c_{gi} L}{\omega A_i} \frac{\tau_{ij}}{2 - \tau_{ij} - \tau_{ji}} \tag{3}$$

The coupling loss factor at a line junction in VA One is thus proportional to $\tau_{ij}/(2-\tau_{ij})$ while the equivalent coupling loss factor at a line joint in Comet Enflow is proportional to $\tau_{ij}/(2-\tau_{ij}-\tau_{ji})$. Without the additional power transmission coefficient τ_{ji} in the EFEA formulation the coupling loss factors are the same and only valid for weakly coupled systems. The VA One and Comet Enflow predicted velocity responses in Bays 5-8 are compared in Figure 19-Figure 22. The energy flow across the ring frames decreases more rapidly for the VA One than for the Comet Enflow predictions and is most notable in the frequency range from 315 to 1250 Hz.

The final structural configuration studied is a full model of the floor-equipped composite cylinder. The VA One predicted root-mean-square velocity responses in bay subsystems X and 5-8, including the beam energies, are shown in Figure 23 while the root-mean-square velocities without the beam responses included in the solution matrix are presented in Figure 24. The Comet Enflow results for the same bays

are shown in Figure 25. Comparisons of the VA One and Comet Enflow predicted root-mean square velocity responses for Bay X and Bays 5-8 in Figure 26 through Figure 30, respectively, show the same trends for the floor-equipped cylinder as found for the fifteen bay subsystems separated by the longitudinal stiffeners and the ring frames discussed previously.

Interior Acoustic Sound Pressure Level Predictions

The sound pressure levels in the acoustic cavity above the floor of the composite cylinder were predicted by VA One and Comet Enflow for unit power input to Bay X. Energy storage and dissipation in the stiffeners were not included in the prediction models. The results are depicted in Figure 31 with VA One predicting sound pressure levels up to 12.8 dB lower than Comet Enflow below the 250 Hz one-third octave band and up to 6.2 dB higher than Comet Enflow above the 250 Hz one-third octave band.

To investigate the discrepancy between the two prediction methodologies a simplified structural-acoustic model was created consisting of a single non-rigid bay (Bay X), defined as the area between two ring frames and two longitudinal stringers, and the acoustic cavity above the floor. Within the VA One model of this two subsystem configuration an area junction was created between the shell bay and the acoustic cavity. A corresponding finite element model of a single non-rigid bay and interior acoustic cavity was imported in Comet Enflow and an area joint was automatically generated between the bay and the interior acoustic space. The applicable geometric, material and damping properties from the previous full composite cylinder models were preserved. The shell bay area in VA One consisted of a singly curved shell subsystem, while the bay area in Comet Enflow was constructed from six plate elements that were connected at an appropriate angle to mimic the curvature of the shell. In both models the curved bay was excited by unit power input. The results are shown in Figure 33 with VA One predicting sound pressure levels up to 5.2 dB lower than Comet Enflow below the 250 Hz one-third octave band and up to 6.7 dB higher than Comet Enflow above the 250 Hz one-third octave band. The character of these discrepancies is similar to the differences in the SEA and EFEA sound pressure level predictions for the full composite cylinder model (Figure 31). The root-mean-square velocities predicted by SEA and EFEA for the curved bay excited by unit input power were virtually identical as shown in Figure 34, suggesting that the coupling between the curved bay and the acoustic cavity is different for the two energy flow methods.

The sound pressure level calculations were repeated for the same model configuration but for a nearly flat bay area instead of a curved bay. For the VA One model this was achieved by replacing the 0.838 m radius of the singly curved shell by a very large number. In EFEA the curvature of the plate group was set to zero. The sound pressure levels were predicted by VA One and Comet Enflow in the acoustic cavity for excitation of the virtually flat plate by unit power input, resulting in almost identical results as shown in Figure 35. The results in Figure 33 and Figure 35 indicate that when curvature is applied to a flat plate the different approaches in VA One (SEA) and Comet Enflow (EFEA) yield different sound pressure level predictions. The methodology followed in VA One as well as Comet Enflow for predicting sound radiation from a curved shell are investigated in the following sections.

VA One curved shell sound radiation prediction

The power Π radiated by a flat plate with length a and width b into the cylinder cavity above the floor is dependent on the space averaged, mean-square velocity $\langle \overline{v^2} \rangle$ of the radiating surface, and the radiation efficiency σ[17]

$$\Pi = \rho_0 c \sigma a b \left\langle \overline{v^2} \right\rangle \tag{4}$$

where ρ_0 is the density of the fluid (air) and c is the speed of sound in the fluid. Above the critical frequency, the lowest frequency at which the speed of the forced bending waves equal the speed of sound in the adjacent fluid, the plate radiates sound from its entire surface into the acoustic far field. At frequencies below the critical frequency the plate radiates sound into the far field by means of edge and corner modes.[18] The critical frequency f_{cr} of an orthotropic plate is defined by[19]

$$f_{cr} = \left[\frac{c^4 \rho_m}{\pi^2 (3+\alpha) \sqrt{D_{11} D_{22}}} \right] \tag{5}$$

where ρ_m is the mass per unit area of the plate. D_{11} and D_{22} are the flexural rigidities in two perpendicular material directions and are given by[19]

$$D_{11,22} = \frac{h^3 E_{11,22}}{12(1-\nu_{12}\nu_{21})} \tag{6}$$

where h is the thickness of the plate, E_{11} and E_{22} are the elasticity moduli along the two main material directions and ν_{12} and ν_{21} are the Poisson ratios. The parameter α is defined in Reference 19 by

$$\alpha = \frac{D_{12} + D_{66}}{\left(D_{11} D_{22}\right)^{0.5}} \tag{7}$$

where D_{12} and D_{66} are flexural rigidity matrix values of the orthotropic plate. If α is not known, two critical frequencies in the primary directions of the laminate can be defined as

$$f_{cr_{1,2}} = \frac{c^2}{2\pi} \sqrt{\frac{\rho_m}{D_{11,22}}} \tag{8}$$

For the cylinder shell material properties listed in Table 2 the two critical frequencies were calculated to occur at 6238 Hz and 6983Hz. Since the frequency range of interest is 100 Hz to 4000 Hz the current analysis is for sound radiation below the critical frequency.

The total number of modes $N(f)$ of a flat orthotropic plate up to a frequency f is given in Reference 20 by

$$N(f) = \frac{abf\sqrt{\rho h}}{\pi} \int_0^{\pi/2} \frac{d\theta}{\sqrt{D(\theta)}} \tag{9}$$

where $D(\theta)$ is the prime material axis polar coordinate dependent flexural rigidity of the flattened orthotropic shell and can be written as[20]

$$D(\theta) = \frac{h^3}{12}\left[E_{11}^{'} \cos^4\theta + 2\left(\nu_{12} E_{22}^{'} + 2G_{12}\right)\cos^2\theta \sin^2\theta + E_{22}^{'} \sin^4\theta \right] \tag{10}$$

where G_{12} is the shear modulus and

$$E'_{11,22} = \frac{E_{11,22}}{1-\nu_{12}\nu_{21}} \tag{11}$$

Lyon[21] simplified the integral in the expression for the number of modes *N(f)* by taking the average of the flexural rigidities along the two prime material directions. The modal density of the flattened orthotropic shell $n_{flat}=dN(f)/df$ can thus be expressed as

$$n_{flat} = \frac{ab\sqrt{\rho h}}{4}\left(\frac{1}{\sqrt{D_{11}}}+\frac{1}{\sqrt{D_{22}}}\right) \tag{12}$$

and is independent of the frequency *f*. The VA One predicted modal density of the flattened orthotropic shell is plotted in Figure 36.

Compared to a flat plate the curved shell is stiffened in the direction of the curvature causing the modes of the shell below the breathing cylinder mode at the ring frequency f_R to resonate at higher frequencies.[22] The shell curvature effects are important below the ring frequency f_R while the shell will behave like a flat plate well above the ring frequency.[18] The plane strain ring frequency for a radius of curvature *r* is defined by[23]

$$f_R = \frac{c_{l_2}}{2\pi r} \tag{13}$$

while the longitudinal group speed in the orthotropic shell material along the two prime axes is given by[24]

$$c_{l_{1,2}} = \sqrt{\frac{E_{11,22}}{\rho\left(1-\nu_{12}\nu_{21}\right)}} \tag{14}$$

The ring frequency for the composite cylinder was computed to occur at 1036 Hz. Compared with the modes of a flat plate, the modes of the curved shell shift towards its ring frequency resulting in an increased modal density in that frequency region. An empirically based curve fitting approximation for the curved shell modal density $n_{curved}(f)$ was proposed by Szechenyi[25] for three different one-third octave band regions. The regions are defined in terms of ξ_r, which is the ratio of the frequency *f* over the plane stress ring frequency f_r for which the axial stress component is zero

$$n_{curved}\left(f\right) = \frac{B\left(\xi_r\right)}{2.6} n_{flat} \tag{15}$$

where

$$\xi_r = 2\pi r f \rho / E_{22} \tag{16}$$

for $\xi_r \le 0.48$ $\quad B\left(\xi_r\right) = 2.5\sqrt{\xi_r}$

for $0.48 < \xi_r \le 0.83$ $\quad B\left(\xi_r\right) = 3.6\xi_r$

for $\xi_r > 0.83$ $\quad B\left(\xi_r\right) = 2 + 2.9001\cos\left(1.3861\xi_r^{-2}\right) - 0.8884\cos\left(2.1968\xi_r^{-2}\right)$

Langley[26] evaluated the modal density of a cylinder and obtained a closed form solution in terms of elliptic integrals showing that at high frequencies the modal density of the shell approaches the modal density of a flat plate as predicted by Szechenyi.[25] Lyon and DeJong[15] assessed the mode count of a thin-walled cylinder. A smooth curve fit was applied to the solutions below and above the plane strain ring frequency to avoid the discontinuity around the ring frequency and to obtain a result valid over the entire frequency region. The modal density for a curved shell is expressed by[15]

$$n_{curved}(f) \approx \frac{ab}{4\pi r\kappa}\xi_R\left[1+\left(\frac{\pi}{2\sqrt{\xi_R+\xi_R^{3.5}}}\right)^4\right]^{-1/4} \tag{17}$$

where $\xi_R=f/f_R$ and κ is the radius of gyration for bending. Results for the predictions above compare well with the computational results from the VA One program, which are shown in Figure 36 for the flat plate and the singly curved shell. The VA One computed number of modes in band are listed in Table 6 for the flat and the curved bay subsystem showing the shift of modes towards the ring frequency while the number of modes well above the ring frequency is about the same for the flat and the curved bays.

The radiated power into the acoustic cavity defined previously is not only dependent on the modal density but is also dependent on the radiation efficiency. The radiation efficiency of a flat plate, below the critical frequency, is approximated by[27]

$$\sigma_{rad}(f<f_{cr}) = \frac{a+b}{ab\pi k\mu\sqrt{\mu^2-1}}\left[\ln\left(\frac{1+\mu}{1-\mu}\right)+\frac{2\mu}{\mu^2-1}\right] \tag{18}$$

where $k=2\pi f/c$ is the wave number and the parameter μ equals $(f/f_{cr})^{1/2}$. Below the critical frequency the radiation efficiency decreases with lower frequencies and shorter plate dimensions a and b. The VA One predicted radiation efficiency for the shell subsystem without curvature is shown in Figure 37. All radiating modes in this region are acoustically slow and only radiate through edge and corner modes. Adding curvature to the shell produces the ring frequency. In the region of the ring frequency some of the modes become acoustically fast as their wavelengths are longer than the acoustic wavelength which, in turn, causes an increase in the radiation efficiency. The VA One predicted radiation efficiency of the curved shell is compared with the flat plate radiation efficiency in Figure 37. The SEA coupling loss factor η_{sa} between the structure and the acoustic cavity is related to the radiation efficiency σ_{rad} of the structure[18]

$$\eta_{sa} = \frac{\rho_0 c\sigma_{rad}}{\omega\rho_m} \tag{19}$$

The VA One predicted coupling loss factors for the flattened and the curved shell are presented in Figure 38. The modal density in the acoustic cavity $n_a(\omega)$ is defined as[15]

$$n_a(\omega) = \frac{V}{2\pi^2c^3}\omega^2+\frac{S}{8\pi^2c^2}\omega+\frac{P}{16\pi c} \tag{20}$$

where V is the volume, S is the cavity bounding surface area and P is the perimeter. Applying reciprocity for the energy flow to and from the acoustic cavity results in the coupling loss factor η_{as} from the acoustic cavity to the bay subsystem

$$\eta_{as} = \frac{n_s(\omega)\eta_{sa}}{n_a(\omega)} \tag{21}$$

The VA One predicted acoustic cavity to bay subsystem coupling loss factor for the flattened and curved shell is shown in Figure 39.

The ratio of energy level in the acoustic cavity E_a and the energy level in the shell E_s is related to the coupling loss factors η_{sa} and η_{as}, and the damping loss factor η_a of the acoustic cavity by[15]

$$\frac{E_a}{E_s} = \frac{\eta_{sa}}{\eta_a + \eta_{as}} \tag{22}$$

where

$$\eta_a = \frac{13.816}{\omega T_{60}} \tag{23}$$

and T_{60} is the reverberation time in the acoustic cavity.

The mean square vibrational energy in the shell can be expressed in terms of the mean square velocity

$$E_s = \rho_m ab\left\langle \overline{v^2} \right\rangle \tag{24}$$

and the energy level in the acoustic cavity is related to the mean-square sound pressure

$$E_a = \frac{\left\langle \overline{p^2} \right\rangle V}{\rho_0 c^2} \tag{25}$$

The sound pressure level in the cavity is then given by

$$10\log\left\langle \overline{p^2} \right\rangle = 10\log\left(\frac{\rho_0 c^2 ab\rho_m \left\langle \overline{v^2} \right\rangle}{V} \frac{\eta_{sa}}{\eta_a + \eta_{as}} \right) \tag{26}$$

where

$$\frac{\eta_{sa}}{\eta_a + \eta_{as}} = \frac{\dfrac{2\rho_0 c\sigma}{\omega\rho_m}}{\dfrac{13.816}{\omega T_{60}} + \dfrac{2\pi\sqrt{3}ab\rho_0 c^4\sigma}{c_l h\omega^3 V\rho_m}} \tag{27}$$

The VA One predicted sound pressure level response in the acoustic cavity due to the unit power input for the flattened and curved bay subsystem is presented in Figure 40.

Comet Enflow curved shell sound radiation prediction

The EFEA power transmission coefficient τ_{sa} from a plate into an acoustic space is defined by[28]

$$\tau_{sa} = \frac{2\omega h \eta_{rad}}{c_{gf} + \omega h \eta_{rad}} \tag{28}$$

where η_{rad} is the radiation damping loss factor and c_{gf} is the flexural wave group velocity. The EFEA power transmission coefficient from the acoustic space into the structure is discussed in Reference 8

$$\tau_{as} = \frac{4\pi c^2 \eta_{rad}}{c_{gf}^2} \zeta(\omega) \tag{29}$$

where the coefficient $\zeta(\omega)$ is defined by[8]

$$\zeta(\omega) = \frac{\frac{V}{2\pi^2 c^3}\omega^2}{\frac{V}{2\pi^2 c^3}\omega^2 + \frac{S}{8\pi^2 c^2}\omega + \frac{P}{16\pi c}} \tag{30}$$

with V being the volume of the acoustic cavity, S the total surface surrounding the cavity and P the perimeter of the acoustic cavity. The rotational frequency ω dependent flexural group velocity for a flat orthotropic plate is given by[14]

$$c_{gf} = \sqrt[4]{\frac{D_{12}\omega^2}{\rho_m}} \tag{31}$$

where $D_{12}=\nu_{21}D_{11}+G_{12}h^3/12$. In Comet Enflow the increased stiffness due to the curvature of the shell element is accounted for by adjusting the bending wave speed below the ring frequency.[25] The flat plate flexural group velocity can be written in terms of the modal density n_{flat}

$$c_{gf} = \sqrt{\frac{S\omega}{\pi n_{flat}}} \tag{32}$$

Knowing this relationship the same coefficients[25] as used for the modal density can be employed for the flexural group velocity in Comet Enflow when correcting for the effect of curvature

$$\text{for } \xi_r \le 0.48 \qquad c'_{gf} = \xi_r^{-1/4} c_{gf}$$

$$\text{for } 0.48 < \xi_r \le 0.83 \qquad c'_{gf} = 0.841 \xi_r^{-1/2} c_{gf}$$

for $\xi_r > 0.83$ no correction was applied to the flexural group speed since in Comet Enflow it was assumed that above the ring frequency the curved shell behaves like a flat plate. The radiation damping loss factor η_{rad} for the curved shell was not modified. The effect of curvature on the Comet Enflow predicted sound pressure level inside the acoustic cavity is shown in Figure 41.

Evaluation of the VA One and Comet Enflow interior sound pressure level predictions

Single bay excitation – In the preceding sections the effects of curvature on the sound radiation into the acoustic cavity were analyzed for both the VA One SEA and Comet Enflow EFEA methodologies. The differences in interior sound pressure levels for the excitation of a curved single bay (Figure 33) can be explained by the different approaches in each energy prediction code. The interior predicted sound pressure levels for excitation of a flat single bay result in almost identical predictions (Figure 35).

The trends of the VA One and Comet Enflow sound pressure level predictions for the curved single bay subsystem in Figure 33 are similar to the results obtained for single bay excitation of the full, floor equipped, composite cylinder model in Figure 31. This suggests that the differences in the VA One and Comet Enflow predicted interior sound pressure levels for the floor equipped composite cylinder are caused by the different approaches in the VA One and Comet Enflow theories to account for the energy flow between a curved structure and the acoustic interior space.

Sidewall structure excitation - It was shown in Table 6 for the single bay subsystem that only the one-third octave frequency bands above 500 Hz contained at least two modes. The 500 Hz and lower frequency bands are therefore, strictly, not suitable for energy analysis. To investigate the effect of curvature for a larger radiating area which has more modes at lower frequencies a sidewall structure subsystem was considered with an area as large as fifteen bays, but without any stiffeners. The sidewall structure was connected to the upper acoustic cavity subsystem as shown in Figure 42. The length, the width, the perimeter and the area of the sidewall structure are listed along with the dimensions of the original single bay in Table 7. Table 6 shows that more than two modes are resonant in the flat sidewall structure for all one-third octave bands of 100 Hz and higher while the curved sidewall structure exhibits more than two modes in the one-third octave bands at 125 Hz and above. The VA One and Comet Enflow predicted sound pressure levels in the acoustic cavity, for the unit power excitation applied to the flat or curved sidewall structure, are presented in Figure 43. The VA One and Comet Enflow computed sound pressure levels for the flat sidewall are approximately the same, but the VA One predictions for the curved sidewall structure are up to 12.5 dB higher than the Comet Enflow predictions.

The differences in the predicted SEA and EFEA sound pressure levels with the excitation applied to a single bay or the sidewall structure (flat as well as curved) are shown in Figure 44. The SEA and the EFEA predictions for the flat plate and the EFEA predictions for the curved plate are approximately 5.5 dB higher for the single bay excitation than for the sidewall structure excitation over the entire range of 100 – 4000 Hz one-third octave bands. However, the approximate 5.5 dB difference only applies to the SEA predictions for the curved bay and sidewall excitations above the 1000 Hz one-third octave band. Below this frequency the sound pressure level difference varies between 0 and 1.5 dB (Figure 44).

The differences in interior sound pressure level predicted by Comet Enflow due to the change in area of the excited structure can be explained by evaluating the power transmission coefficients. The EFEA power transmission coefficient τ_{sa} from a plate into an acoustic space can be expressed in terms of the radiation efficiency σ[28]

$$\tau_{sa} = \frac{2\beta\sigma_{rad}}{2+\beta\sigma_{rad}} \tag{33}$$

where $\beta=c\rho_0/c_s\rho_s$ is the ratio of the characteristic impedances of the fluid (air) and the structure. Assuming that $\beta\sigma_{rad} \ll 2$ and only the area of the excited structure is changed, then the power transmission coefficient is dependent on only the radiation efficiency. Below the critical frequency the radiation efficiency, which was defined previously in Equation (18), scales with $(a+b)/ab$. The change in the predicted interior sound pressure levels when exciting the sidewall structure (with an area covering a matrix of five by three bays)

instead of the single bay is then 10log(3+5)/15=5.7 dB. This difference applies to the flat as well as to the curved subsystems.

The interior sound pressure levels differences predicted by VA One in Figure 44, due to the different areas of the single bay and the sidewall structure, can be explained by evaluating the previously presented expression for the interior sound pressure levels in Equation (26). Assuming that the SEA coupling loss factor η_{as} (Figure 39) is much smaller than the damping loss factor η_a of the acoustic cavity (Table 5), the ratio of $\eta_{sa}/(\eta_a+\eta_{as})$ becomes almost equal to η_{sa}/η_a. The acoustic cavity sound pressure level then can be rewritten as

$$10\log\left\langle \overline{p^2} \right\rangle \cong 10\log\left(\frac{2\rho_0^2 c^3 T_{60}}{13.816 * V} ab \left\langle \overline{v^2} \right\rangle \sigma \right) \tag{34}$$

In this equation, for the same unit power excitation of the single bay or the sidewall structure (fifteen times the area of the single bay), the product of the area ab and the mean-square velocity $\langle \overline{v^2} \rangle$ is about constant and the sound pressure level in the acoustic cavity scales with approximately ten times the logarithm of the radiation efficiency or 10log(σ). The VA One predicted radiation efficiencies for the flat and curved sidewall structures are shown in Figure 45. The VA One predicted sound pressure levels for the single bay in Figure 40 and for the sidewall structure in Figure 43 can thus be explained by the radiation efficiency curves in Figure 37 and Figure 45, respectively. The approximation of ten times the logarithm of the radiation efficiency ratio for the sound pressure level differences in the acoustic cavity for the single bay or sidewall structure excitation is illustrated in Figure 46 to be very close to the sound pressure level differences computed by the VA One prediction program.

CONCLUSIONS

Statistical Energy Analysis (VA One) and Energy Finite Element Analysis (Comet Enflow) response predictions were made for a floor-equipped composite cylinder excited by a unit power input on a bay subsystem bounded by two longitudinal stringers and two ring stiffeners. The input to the prediction codes, including mechanical material properties, geometrical characteristics and damping loss factors, was the same for both energy methods. The forced transmission loss path for the floor was not included. and the flexural, extensional and torsional energy storage and dissipation in the stiffeners were not modeled. The VA One predicted root-mean-square velocity in the bay excited by the unit power was similar to the root-mean-square velocity predicted by Comet Enflow.

A sidewall structure with an area the size of fifteen bays was initially considered to be a single subsystem and stringers and ring frames were not included in the analysis. Root-mean-square velocity responses at nodes away from the unit input power node were predicted by Comet Enflow and were compared to the VA One predictions in the 200 Hz and 2000 Hz one-third octave bands. While VA One produces a single estimate for a subsystem, the root-mean square velocity responses predicted by Comet Enflow vary as function of location within the subsystem.

The structural response of a configuration including fifteen bay subsystems separated by the longitudinal stiffeners and the ring frames was evaluated. Comet Enflow considers the beams to not take energy and therefore the VA One bay velocities were predicted excluding the beam energies in the solution matrix. The energy flow across the ring frames to bays away from the excitation bay decreased more rapidly for the VA One than for the Comet Enflow predictions. A possible explanation was offered by the fact that

the coupling loss factor at a line junction in SEA is proportional to $\tau_{ij}/(2-\tau_{ij})$ while the equivalent coupling loss factor at a line joint in EFEA is proportional to $\tau_{ij}/(2-\tau_{ij}-\tau_{ji})$.

The VA One predicted sound pressure levels inside the upper acoustic cavity of the composite cylinder were higher than the Comet Enflow computed levels in one-third octave bands below 250 Hz, while the VA One predictions were lower at the higher frequency bands. Similar trends were observed in a simple two-subsystem configuration, consisting of a curved single bay shell and the acoustic cavity. The differences in the VA One and Comet Enflow interior sound pressure level predictions were shown to be caused by the way the curvature of the shell is incorporated in the VA One and Comet Enflow theoretical analyses. While the VA One implementation of the curvature is based on the modal density of the structure, the curvature in Comet Enflow is addressed by adjusting the bending wave speed in the structure below the ring frequency. The different curvature implementations cause large differences (up to 12.5 dB) in the predicted interior sound pressure levels below and just above the ring frequency. At frequencies well above the ring frequency both interior sound pressure level predictions converge as the structure can be modeled progressively like a flat plate.

REFERENCES

1. Grosveld, F. W., and Beyer, T. B., Modal Characteristics of a Stiffened Cylinder with Open and Closed End Conditions. AIAA 86-1908, AIAA 10th Aeroacoustics Conference, Seattle, Washington, July 9-11, 1986.
2. Beyer, T. B. and Grosveld, F. W., Validation of an Interior Noise Prediction Model for a Composite Cylinder. AIAA-87-0529, AIAA 25th Aerospace Sciences Meeting, Reno, Nevada, January 12-15, 1987.
3. Grosveld, F. W. and Beyer, T. B., Vibratory Response of a Stiffened, Floor-Equipped, Composite Cylinder. *Proceedings of the 5th International Modal Analysis Conference*, London, England, April 6-9, 1987, pp. 812-820.
4. Grosveld, F. W., Sullivan, B. and Marulo, F., Aircraft Interior Noise Prediction Using a Structural Acoustic Analogy in NASTRAN Modal Synthesis. *Proceedings of the 6th International Modal Analysis Conference*, Orlando, FL, February 1-4, 1988, pp. 1191-1198.
5. Beyer, T. and Silcox, R., Noise Transmission of a Large Scale Composite Fuselage Model. AIAA-90-3965, AIAA 13th Aeroacoustics Conference, Tallahassee, Florida, October 22-24, 1990.
6. Grosveld, Ferdinand W., Noise Reduction of a Composite Cylinder Subjected to Random Acoustic Excitation. AIAA-89-1049, AIAA 12th Aeroacoustics Conference, San Antonio, TX, April 10-12, 1989.
7. Jackson, A. C., Balena, F. J., Labarge, W. L., Pei, G., Pitman, W. A. and Wittlin, G., Transport Composite Fuselage Technology: Impact Dynamics and Acoustic Transmission. NASA-CR-4035, December 1986.
8. Grosveld, Ferdinand W., Schiller, Noah H., Cabell, Ran H, "Comparison of Comet Enflow and VA One Acoustic-to-Structure Power Flow Predictions," NASA/TM-2010-216191, February 2010, 51p.
9. Grosveld, Ferdinand W., Schiller, Noah H., Cabell, Ran H, "Finite Element Models and Properties of a Stiffened Floor-Equipped Composite Cylinder," NASA/TM-2010-216192, February 2010, 33p.
10. Cabell, Randolph, Klos, Jake, Buehrle, Ralph and Schiller, Noah, "Vibroacoustic Response Data of Stiffened Panels and Cylinders," *Proceedings of Noise-Con 2008*, Dearborn, Michigan, July 28-31, (2008).

11. Cabell, Randolph, Schiller, Noah, Allen, Albert and Moeller, Mark, "Loss Factor Estimation Using the Impulse Response Decay Method on a Stiffened Structure," *Proceedings of Inter-Noise 2009*, Ottawa, Canada, August 23-26, (2009).
12. Schiller, Noah, Cabell, Randolph and Grosveld, Ferdinand, "Impact of Damping Uncertainty on SEA Model Response Variance," *Proceedings of Noise-Con 2010*, Baltimore, Maryland, April 19-21, (2010).
13. VA One User's Guide. ESI Group North America, San Diego, 2007.
14. Comet Enflow User's Manual. Comet Technology Corporation, Ann Arbor, MI, 2007.
15. Lyon, Richard H. and DeJong, Richard G., "*Theory and Application of Statistical Energy Analysis*," Second Edition, Butterworth-Heinemann, Newton, Massachusetts, 1995.
16. Wang, S. and Bernhard, R. J., "Prediction of Averaged Energy for Moderately Damped Systems with Strong Coupling," *Journal of Sound and Vibration* **319**(3), 2009, pp. 426-444.
17. Fahy, F. J., "Response of a Cylinder to Random Sound in the Contained Fluid," *Journal of Sound and Vibration* **13**(2), 1970, pp. 171-194.
18. Fahy, Frank and Gardonio, Paolo, "Sound and Structural Vibration," Second Edition, Elsevier Academic Press, Amsterdam, 2007.
19. Renji, K. and Nair, P. S., "Critical and Coincidence Frequencies of Flat Panels," *Journal of Sound and Vibration* **205**(1), 1997, pp. 19-32.
20. Bosmans, I., Mees, P. and Vermeir, G., "Structure-Borne Sound Transmission Between Thin Orthotropic Plates: Analytical Solutions," *Journal of Sound and Vibration* **191**(1), 1996, pp. 75-90.
21. Lyon, R. H., "*Statistical Energy Analysis of Dynamic Systems*," Cambridge, Massachusetts, MIT Press, 1975.
22. Lyon, Richard H., "*Designing for Product Sound Quality*," CRC Press, Mechanical Engineering Series, ISBN 0824704002, June 2000.
23. Manning, Jerome E. and Maidanik, Gideon, "Radiation Properties of Cylindrical Shells," *Journal of the Acoustical Society of America*, Volume 36, Number 9, September 1964.
24. Spintsis, I. A., "Determination of the Physicomechanical Characteristics of Viscoelastic Materials in Orthotropic and Isotropic Layers from the Propagation Velocities and Damping Constants of Longitudinal and Shear Vibrations," *Mekhanica Polimerov*, Vol. 3, No. 1, 1967, pp. 161-166.
25. Szechenyi, E., "Modal Densities and Radiation Efficiencies of Unstiffened Cylinders Using Statistical Methods," *Journal of Sound and Vibration* **19**(1), 1971, pp. 65-81.
26. Langley, R. S., "The Modal Density and Mode Count of Thin Cylinders and Curved Panels," *Journal of Sound and Vibration* **169**(1), 1994, pp. 43-53.
27. Leppington, F. G., Broadbent, E.G. and Heron, K. H., "Acoustic Radiation from Rectangular Panels with Constrained Edges," *Proc. R. Soc. Lond.* A **393**, 1984, pp.67-84.
28. Bitsie, F., "The Structural acoustic Energy Finite Element Method and Energy Boundary Element Method.

TABLES

Table 1. Volume, bounding area and total perimeter of the acoustic cavities above and below the floor.

Acoustic Cavity	**Volume** [m^3]	**Area** [m^2]	**Perimeter** [m]
Above the floor	5.83	20.79	24.26
Below the floor	2.25	14.37	21.82

Table 2. Mechanical material properties of the composite cylinder components.

Mechanical Material Properties		**E11** [GPa]	**E22** [GPa]	**G12** [GPa]	**ρ** [kg/m3]	**v12**	**v21**
Cylinder shell	Composite	40.6	32.4	32.2	1590	0.629	0.502
Ring frame 'J' stiffeners	Composite	72.7	28.8	18.3	1574	0.753	0.298
Longitudinal 'Hat' stringers	Composite	95.8	22.9	19.1	1590	0.588	0.141
Aluminum floor beams and floor supports	Isotropic	70.0		26.0	2700	0.30	
Plywood floor	Isotropic	12.4		4.66	711	0.33	
Medium-density fiberboard (MDF) endcaps	Isotropic	2.8		1.037	730	0.35	

Table 3. Beam section properties.

Property Parameter	**Label**		**Floor Beams**	**Floor Supports**	**Longitudinal Stringers**	**Ring Frames**
Shape			'U'	'U'	'Hat'	'J'
Cross sectional area	A	[m^2]	0.0002607052	0.0002607052	0.0001330128	0.0001864582
Moments of inertia	Ixx	[m^4]	1.515540E-08	1.515540E-8	4.538572E-9	7.771676E-8
	Iyy	[m^4]	1.531684E-07	1.531684E-7	2.126092E-8	1.199627E-8
Torsional constant	J	[m^4]	4.96766E-10	4.96766E-10	1.891524E-10	2.209614E-10
Distance shear center	horizontal	[m]	1.318182E-8	1.318182E-8	2.855553E-7	-0.008786919
to centroid	vertical	[m]	-0.01378559	-0.01378559	0.007624588	-0.007008278
Shear stiffness factors	K1		0.2574783	0.2574783	0.2609327	0.3591745
	K2		0.4953249	0.4953249	0.4140227	0.4492481

Table 4. Isotropic mechanical material properties for modeling the composite beam components in VA One.

Mechanical Material Properties		**E11** [GPa]	**G12** [GPa]	**ρ** [kg/m3]	**v12**
Ring frame 'J' stiffeners	Isotropic	48.8	16.3	1574	0.499
Longitudinal 'Hat' stringers	Isotropic	60.3	20.1	1590	0.499

Table 5. Damping loss factors for the main subsystems of the floor-equipped composite cylinder.

One-third Octave Band Center Frequency [Hz]	Shell (flexure) [-]	Floor (flexure) [-]	Upper Acoustic Cavity [-]	Lower Acoustic Cavity [-]
100	0.079	0.076	0.0226297	0.0226297
125	0.174	0.076	0.0242013	0.0242013
160	0.207	0.076	0.0344726	0.0344726
200	0.187	0.076	0.0264031	0.0264031
250	0.185	0.076	0.0190452	0.0190452
315	0.105	0.076	0.0184962	0.0184962
400	0.038	0.08	0.0160743	0.0160743
500	0.09	0.081	0.0155026	0.0155026
630	0.056	0.066	0.0151923	0.0151923
800	0.064	0.074	0.0126923	0.0126923
1000	0.038	0.074	0.00938272	0.00938272
1250	0.028	0.068	0.007705	0.007705
1600	0.036	0.066	0.00613358	0.00613358
2000	0.043	0.064	0.00435032	0.00435032
2500	0.034	0.07	0.0035221	0.0035221
3150	0.041	0.062	0.00250785	0.00250785
4000	0.041	0.060	0.00227444	0.00227444

Table 6. VA One computed modes in band for a single bay and the sidewall structure (fifteen times the area of the single bay), with and without curvature.

One-third Octave Band Center Frequency [Hz]	Single Bay (flat) [-]	Single Bay (curved) [-]	Sidewall Structure (flat) [-]	Sidewall Structure (curved) [-]
100	0.4	0.1	5.5	1.6
125	0.5	0.2	7.0	2.3
160	0.6	0.2	8.9	3.3
200	0.7	0.3	11.1	4.7
250	0.9	0.4	14.0	6.7
315	1.2	0.6	17.6	9.6
400	1.5	0.9	22.2	13.9
500	1.8	1.3	27.7	20.2
630	2.3	2.0	35.2	30.6
800	2.9	3.3	44.1	49.0
1000	3.7	5.4	55.7	81.6
1250	4.7	5.4	70.1	81.7
1600	5.9	6.4	87.9	95.4
2000	7.4	7.8	111.1	116.4
2500	9.3	9.6	139.5	143.5
3150	11.7	11.9	175.9	179.0
4000	14.8	14.9	221.4	223.8

Table 7. Length, width, area and perimeter values for a single bay and for the sidewall structure (fifteen times the area of the single bay).

Structural Component	Length [m]	Width [m]	Perimeter [m]	Area [m^2]
Single bay	0.381	0.240	1.241	0.091
Sidewall structure (15x area single bay)	1.905	0.719	5.248	1.367

Table 8. Flat and curved logarithmic radiation efficiency ratios of a single bay and the sidewall structure (fifteen times the bay area).

One-third Octave Band Center Frequency [Hz]	Radiation Efficiency (flat) Bay [-]	Radiation Efficiency (flat) Sidewall [-]	10log (Bay/Sidewall) (flat) [dB]	Radiation Efficiency (curved) Bay [-]	Radiation Efficiency (curved) Sidewall [-]	10log (Bay/Sidewall) (curved) [dB]
100	0.008393	0.002683	5.0	0.005132	0.677799	0.1
125	0.009330	0.003050	4.9	0.006624	0.004981	0.1
160	0.012427	0.003538	5.5	0.012795	0.006483	1.5
200	0.013385	0.004020	5.2	0.015906	0.008983	1.2
250	0.014695	0.004519	5.1	0.020462	0.012000	0.8
315	0.016483	0.005099	5.1	0.027977	0.017214	0.1
400	0.018920	0.005722	5.2	0.041888	0.027562	-0.2
500	0.021918	0.006489	5.3	0.064878	0.044266	0.0
630	0.025951	0.007450	5.4	0.08793	0.064223	-0.4
800	0.031222	0.008610	5.6	0.14944	0.095874	-0.3
1000	0.037065	0.009970	5.7	0.181283	0.158383	4.5
1250	0.043775	0.011695	5.7	0.071405	0.063786	5.2
1600	0.052952	0.014273	5.7	0.066974	0.021734	5.4
2000	0.064075	0.017573	5.6	0.073718	0.019316	5.5
2500	0.080843	0.022492	5.6	0.088578	0.020986	5.5
3150	0.111502	0.031133	5.5	0.118805	0.025143	5.5
4000	0.178355	0.050359	5.5	0.187725	0.033563	5.5

FIGURES

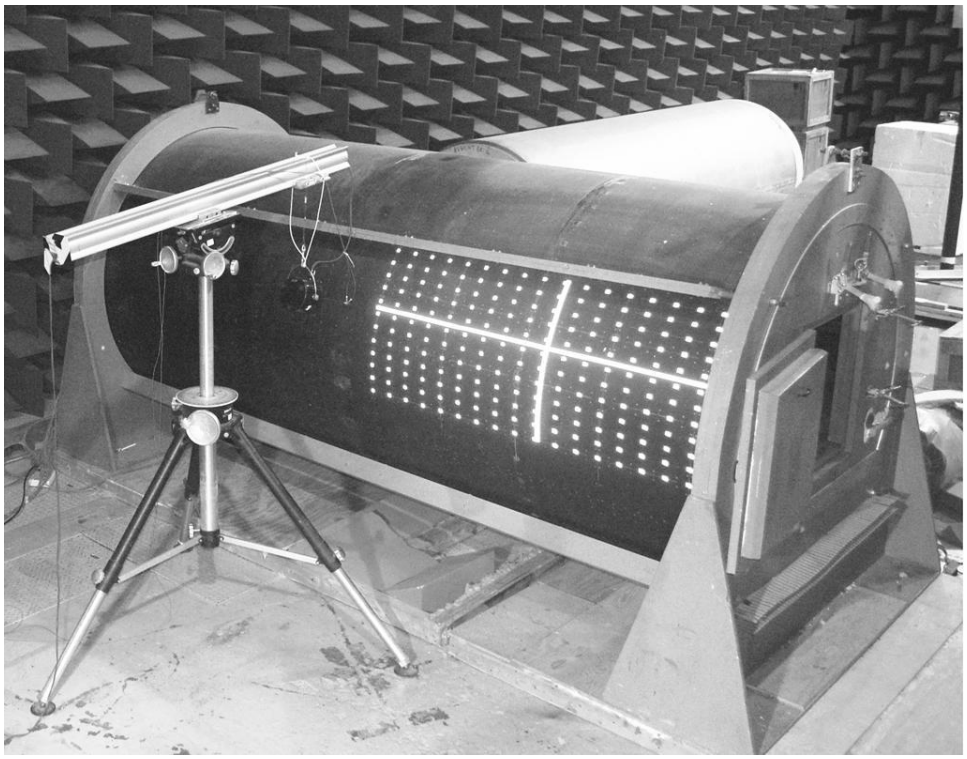

Figure 1. Composite cylinder supported by two endcaps and held together by wood covered (to provide damping) tension rods.

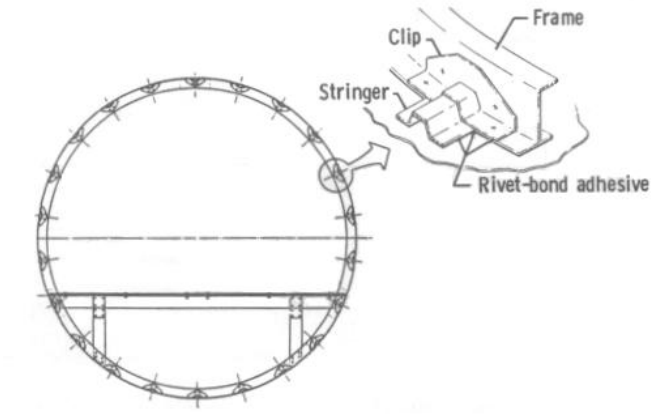

Figure 2. Cross-section of the stiffened, floor-equipped composite cylinder and a detailed view of the rivet-bonded frame-stringer-shell intersection.

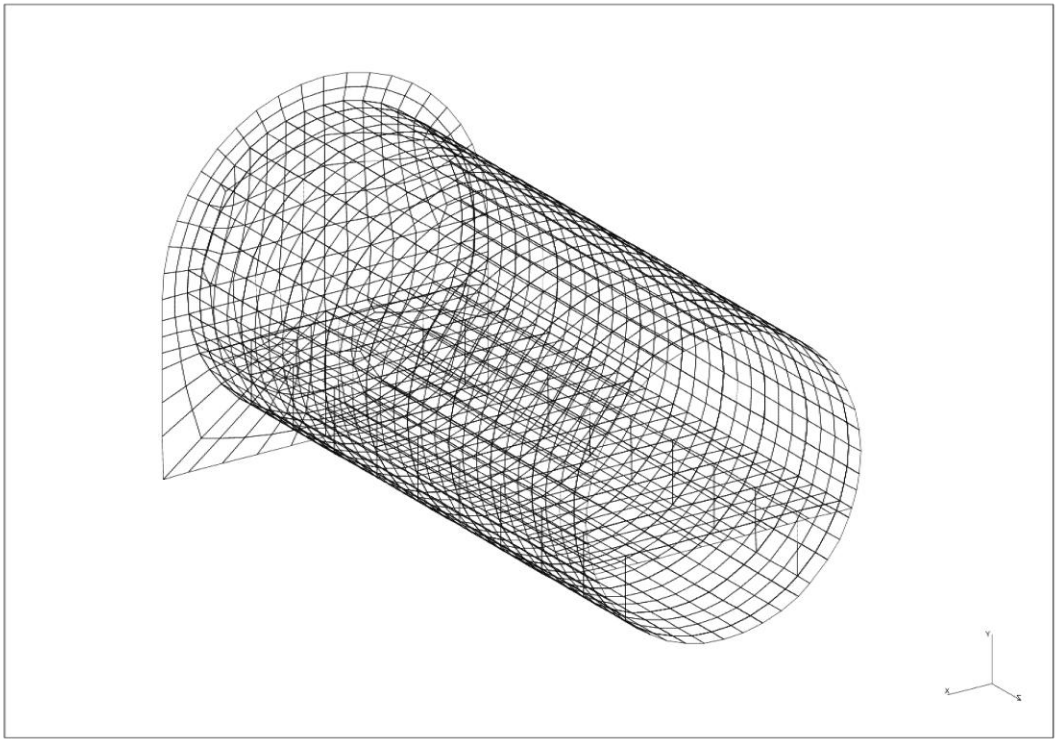

Figure 3. Wireframe isometric view of the floor-equipped composite cylinder energy finite element model with one endcap removed for clarity.

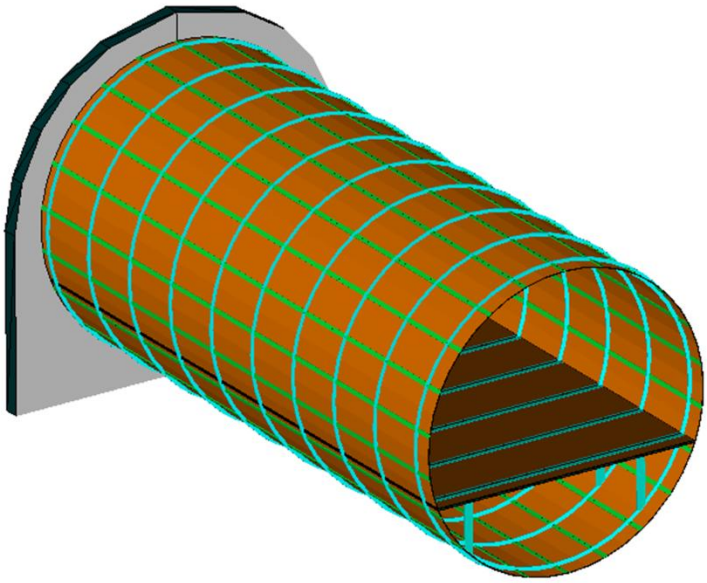

Figure 4. VA One (SEA) model of the floor-equipped stiffened composite cylinder without the front endcap and the acoustic cavity subsystems.

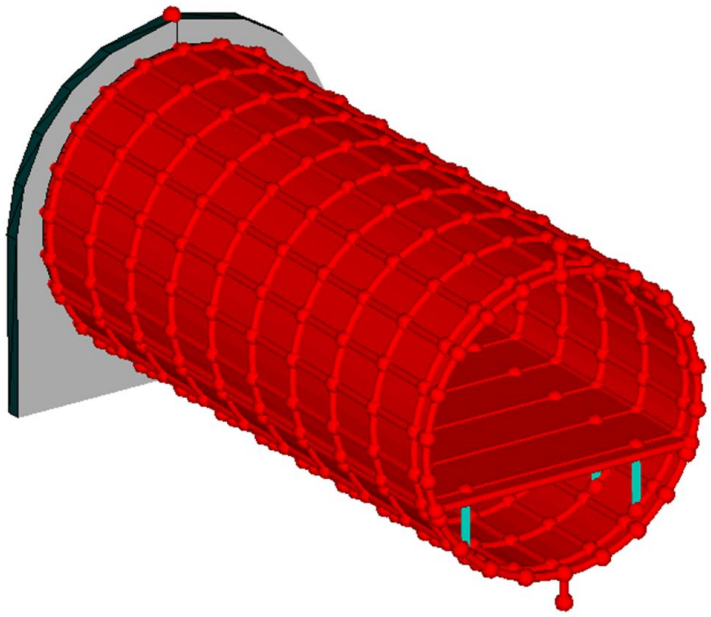

Figure 5. VA One area, line and point junctions with the area junctions between the acoustic cavities and the front endcap removed for clarity.

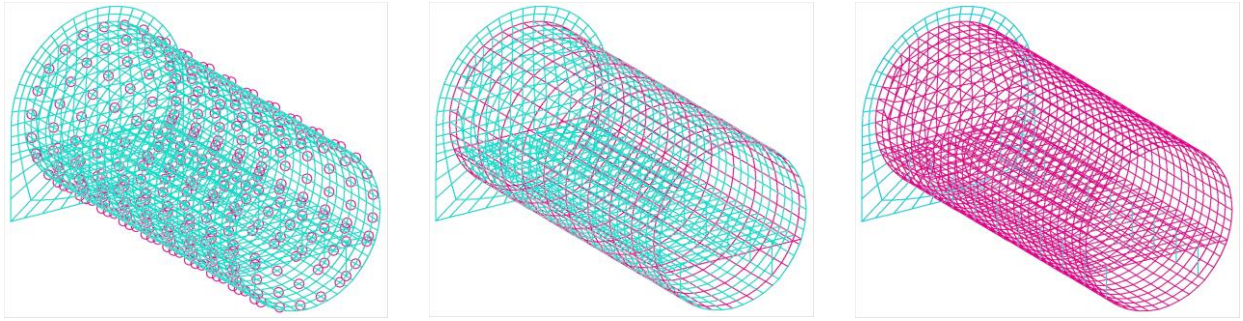

a) point joints b) line joints c) area joints

Figure 6. Comet Enflow point, line and area joints of the composite cylinder energy finite element model.

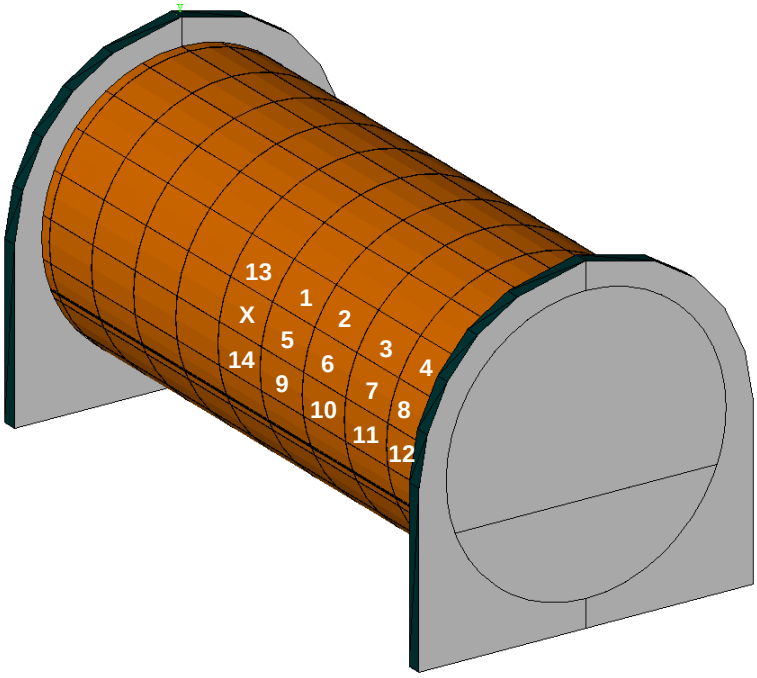

Figure 7. The unit power excitation bay (X) and the fourteen response bays (1-14).

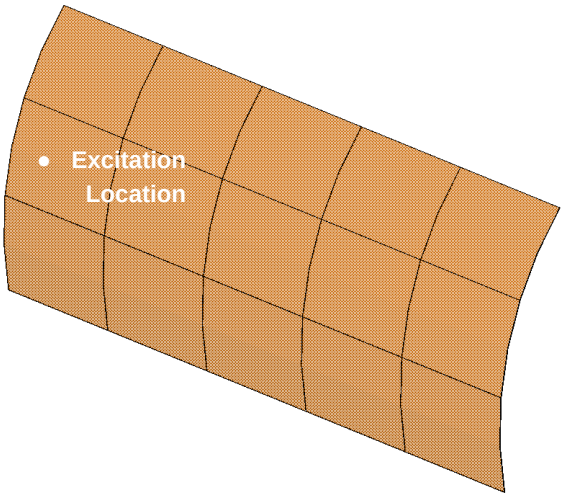

Figure 8. Sidewall structure subsystem (area of fifteen bays).

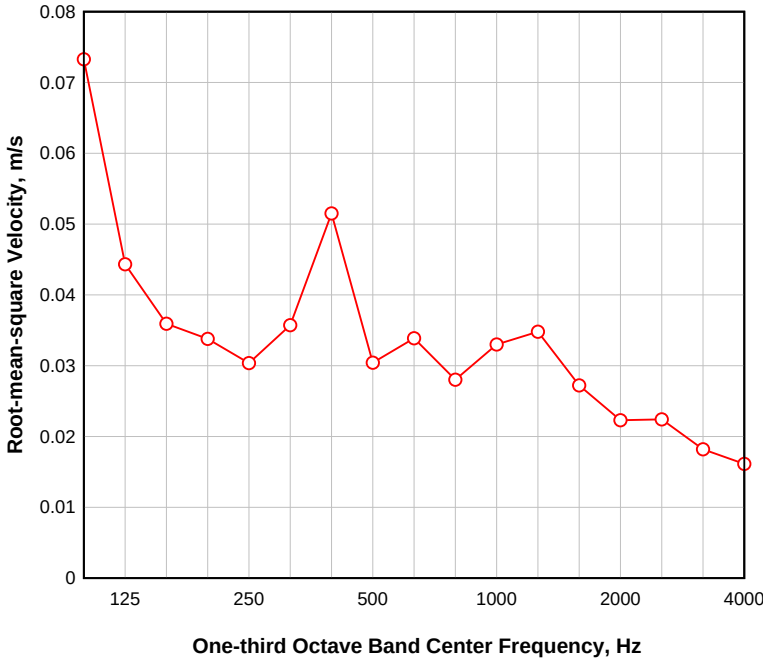

Figure 9. VA One (SEA) root-mean-square velocity predictions on the sidewall structure (same at all locations).

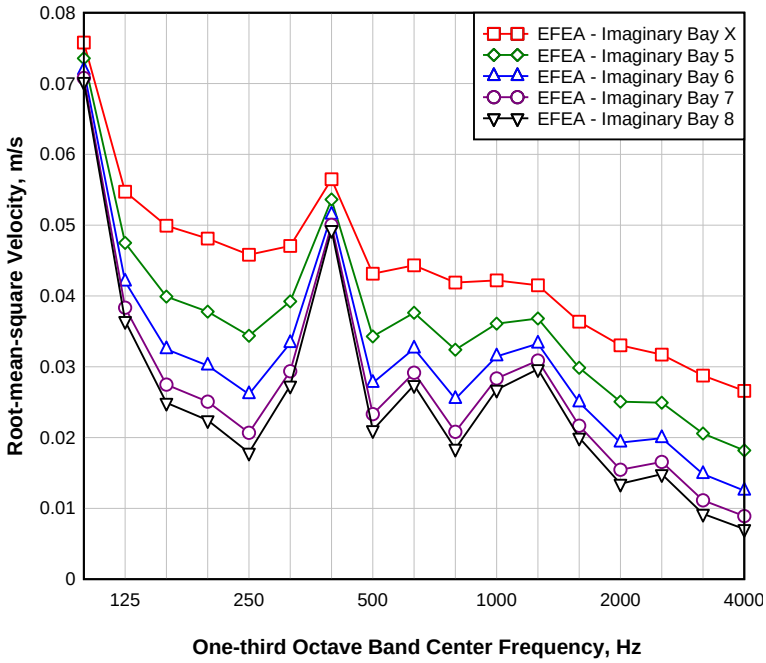

Figure 10. Comet Enflow (EFEA) root-mean-square velocity predictions in the imaginary bays (X and 5-8) of the sidewall structure subsystem.

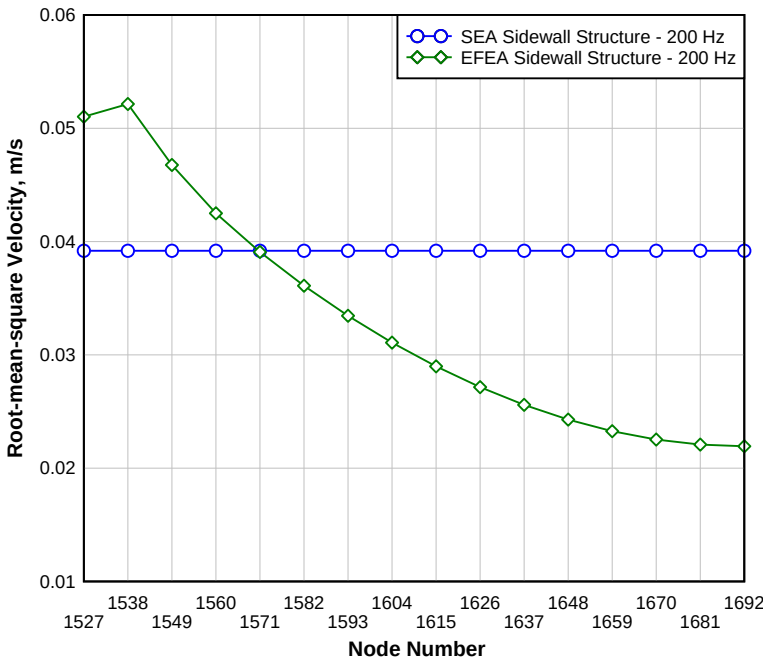

Figure 11. Comet Enflow (EFEA) predicted root-mean-square velocities at nodes away from the unit input power at Node #1538 compared to VA One (SEA) predictions for the sidewall structure subsystem and five smaller bay subsystems in the 200 Hz one-third octave band.

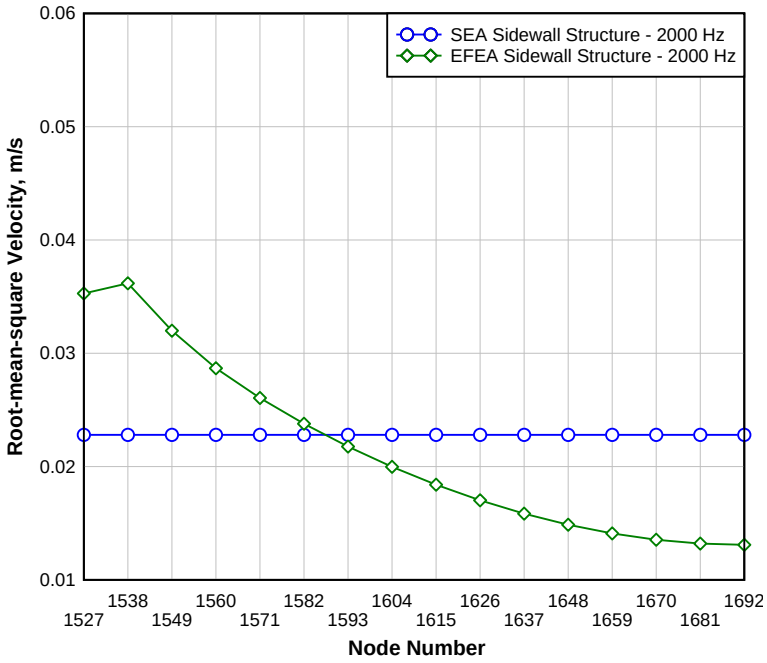

Figure 12. Comet Enflow (EFEA) predicted root-mean-square velocities at nodes away from the unit input power at Node #1538 compared to VA One (SEA) predictions for the sidewall structure subsystem and five smaller bay subsystems in the 2000 Hz one-third octave band.

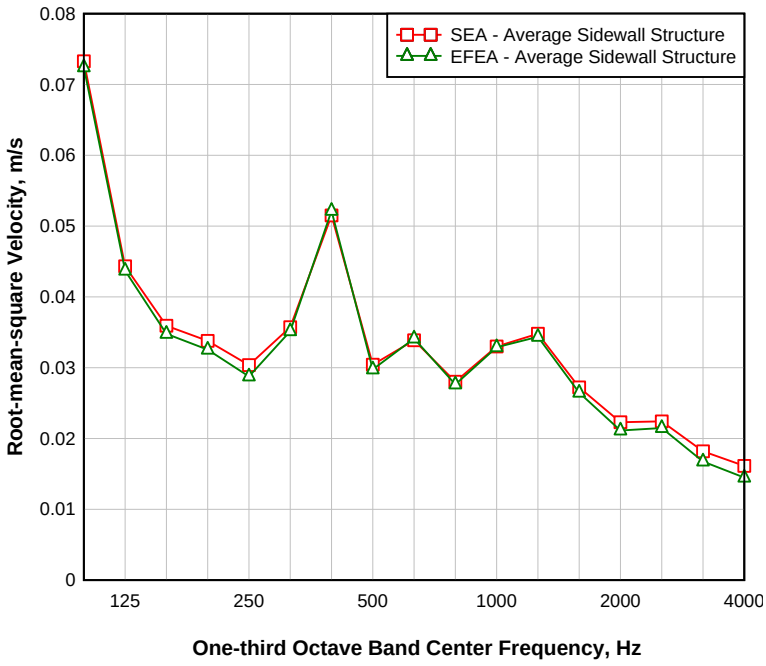

Figure 13. VA One (SEA) and Comet Enflow (EFEA) area averaged root-mean-square velocity predictions of the sidewall structure

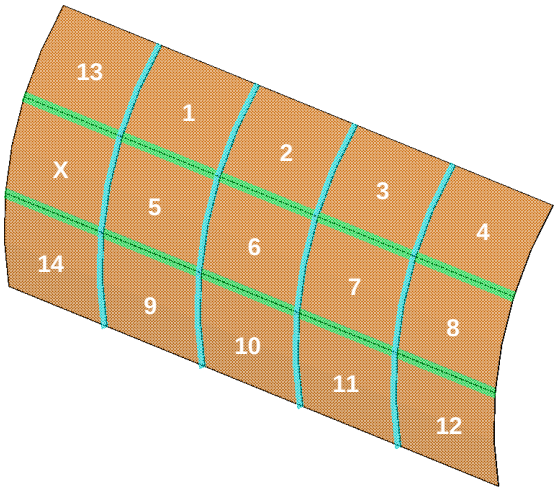

Figure 14. Sidewall structure divided into fifteen bay subsystems by longitudinal stringers and ring frames.

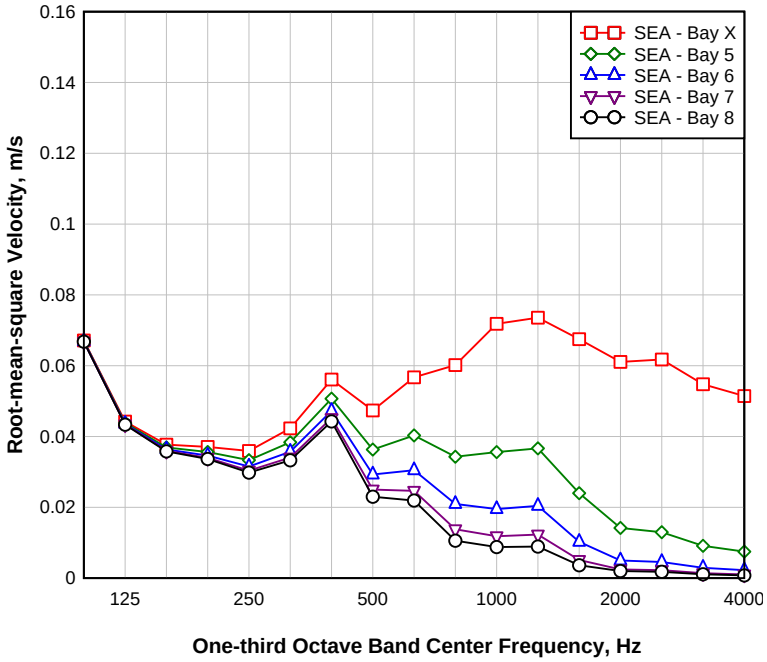

Figure 15. VA One (SEA) root-mean-square velocity predictions for the fifteen bay subsystems separated by longitudinal stringers and ring frames.

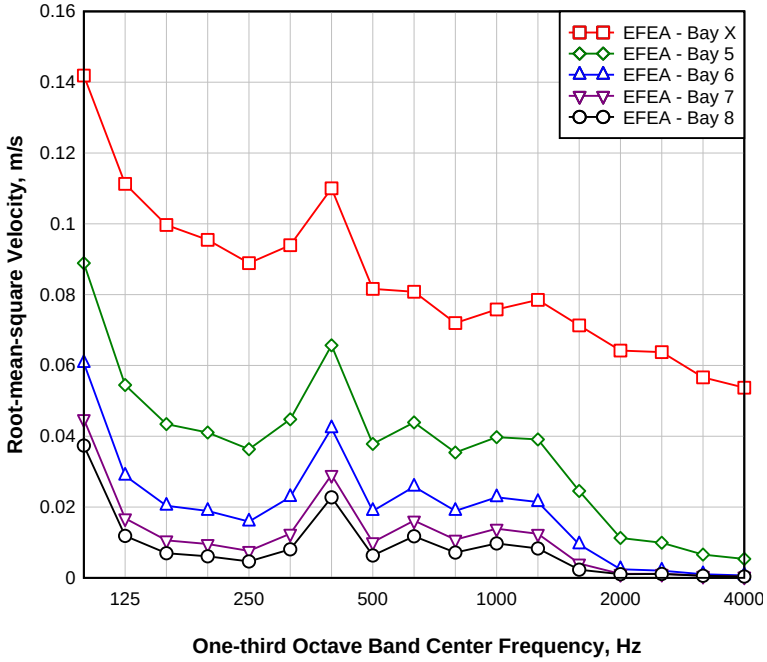

Figure 16. Comet Enflow (EFEA) predicted root-mean-square velocities of the sidewall structure including the longitudinal stringers and ring frames.

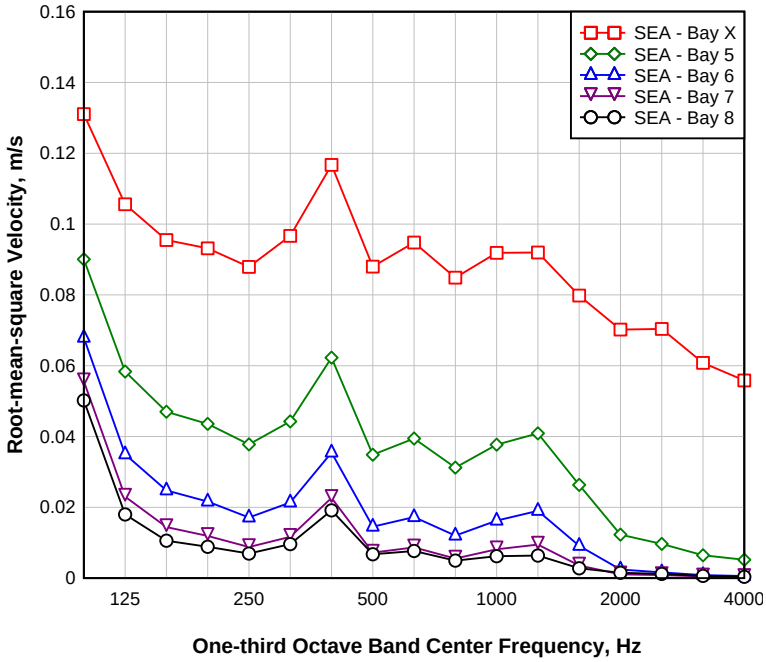

Figure 17. VA One (SEA) root-mean-square velocity predictions for the fifteen bay subsystems separated by longitudinal stringers and ring frames but their responses excluded in the solution matrix.

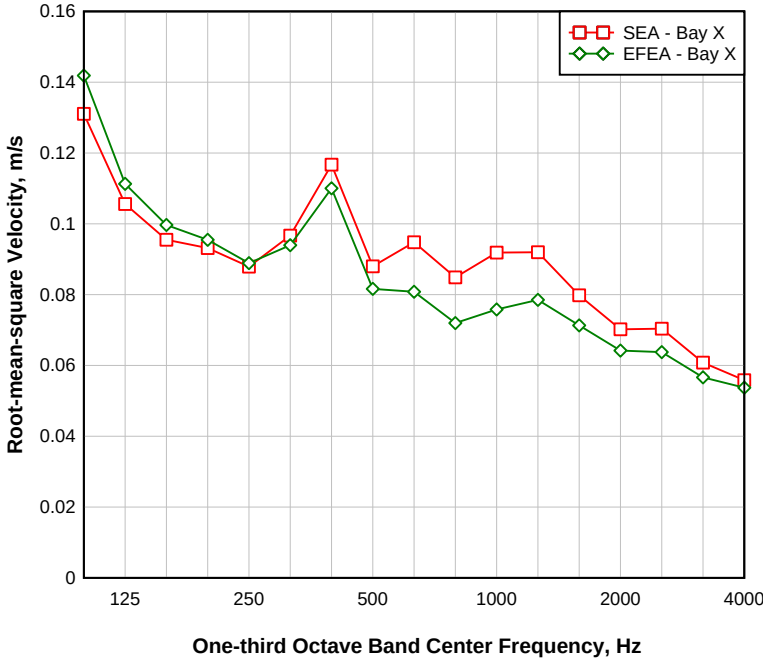

Figure 18. VA One (SEA) and Comet Enflow (EFEA) predicted bay subsystem X root-mean-square velocities for bay subsystems separated by longitudinal stringers and ring frames.

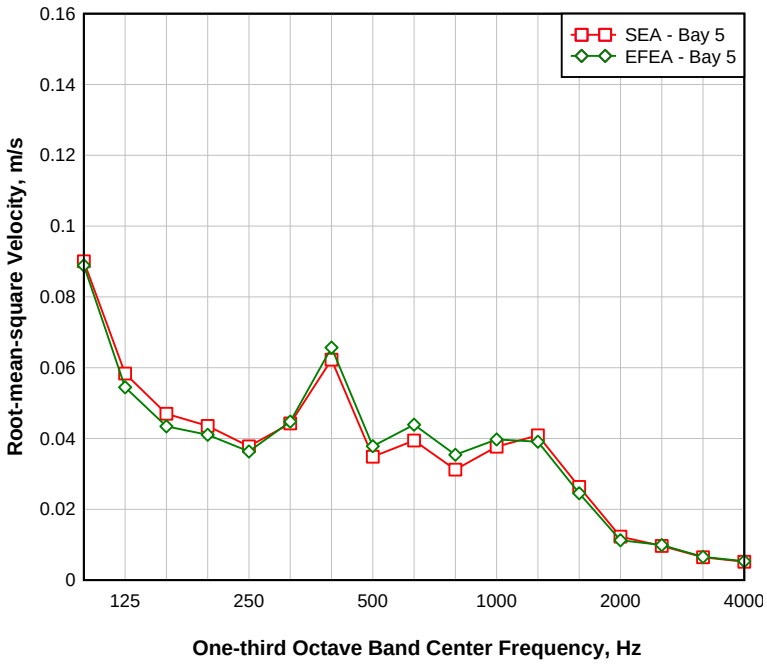

Figure 19. VA One (SEA) and Comet Enflow (EFEA) predicted bay subsystem 5 root-mean-square velocities for the bay subsystems separated by longitudinal stringers and ring frames.

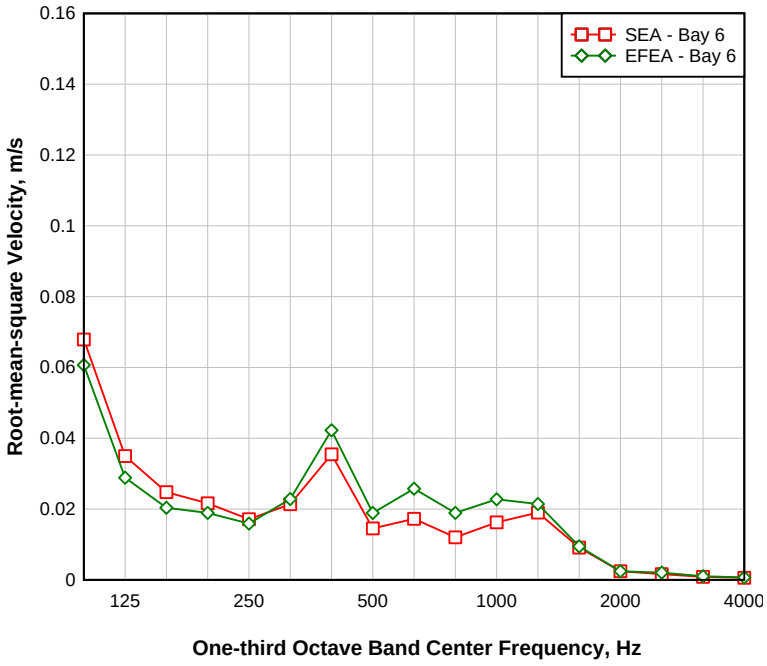

Figure 20. VA One (SEA) and Comet Enflow (EFEA) predicted bay subsystem 6 root-mean-square velocities for the bay subsystems separated by longitudinal stringers and ring frames.

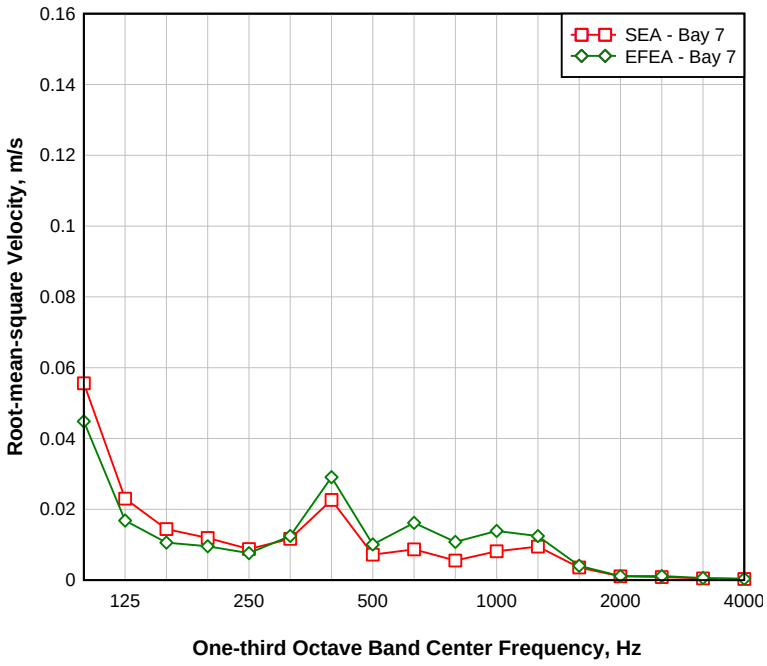

Figure 21. VA One (SEA) and Comet Enflow (EFEA) predicted bay subsystem 7 root-mean-square velocities for the bay subsystems separated by longitudinal stringers and ring frames.

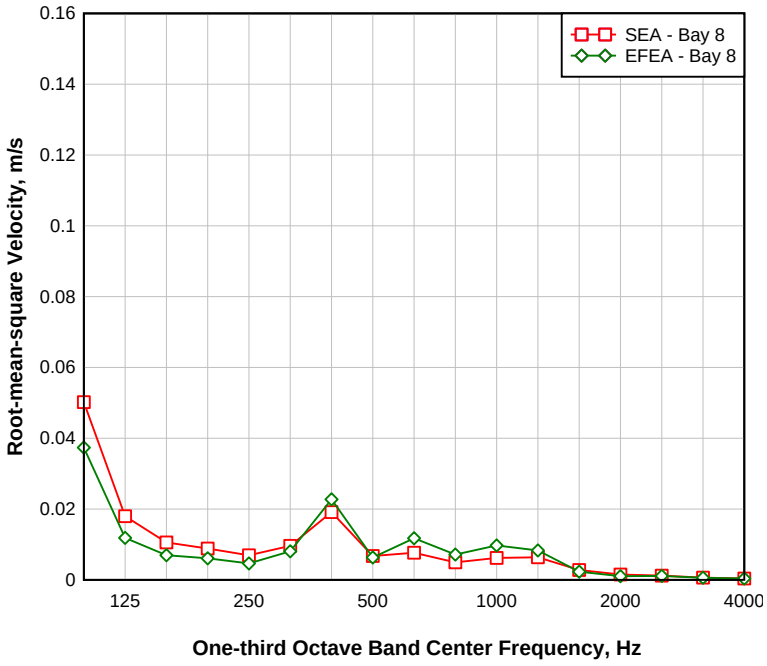

Figure 22. VA One (SEA) and Comet Enflow (EFEA) predicted bay subsystem 8 root-mean-square velocities for the bay subsystems separated by longitudinal stringers and ring frames.

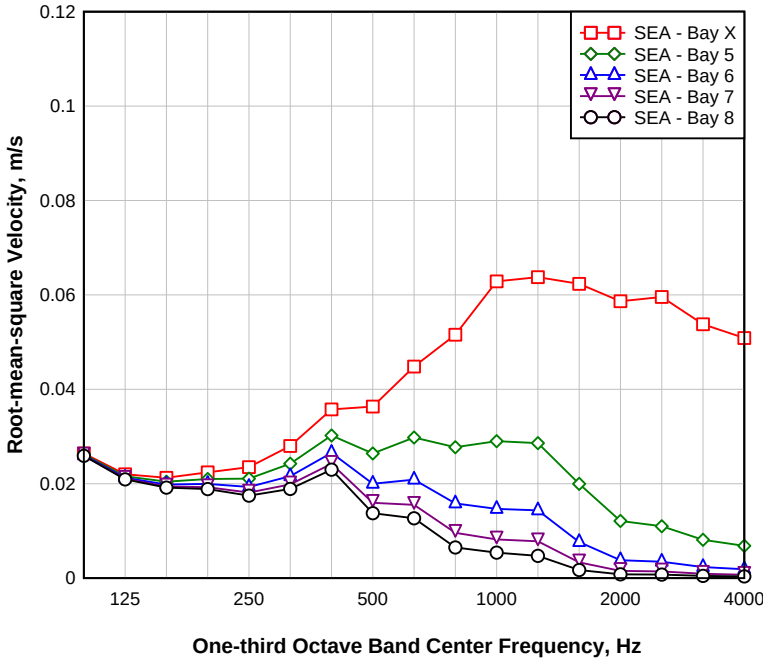

Figure 23. VA One (SEA) predicted root-mean-square velocity responses in bay subsystems X, 5-8 of the floor-equipped composite cylinder.

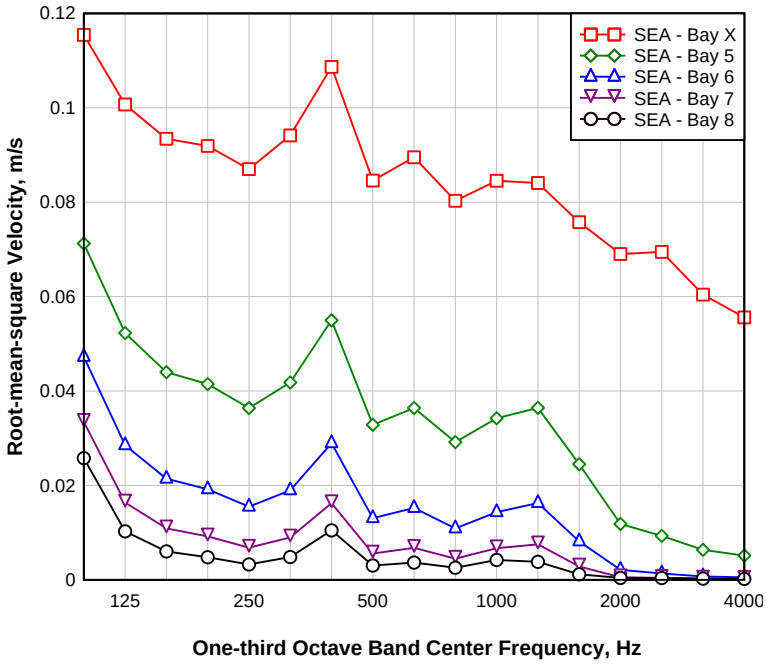

Figure 24. VA One (SEA) predicted root-mean-square velocities in the bay subsystems X, 5-8 of the floor-equipped composite cylinder without the beam responses in the SEA solution matrix.

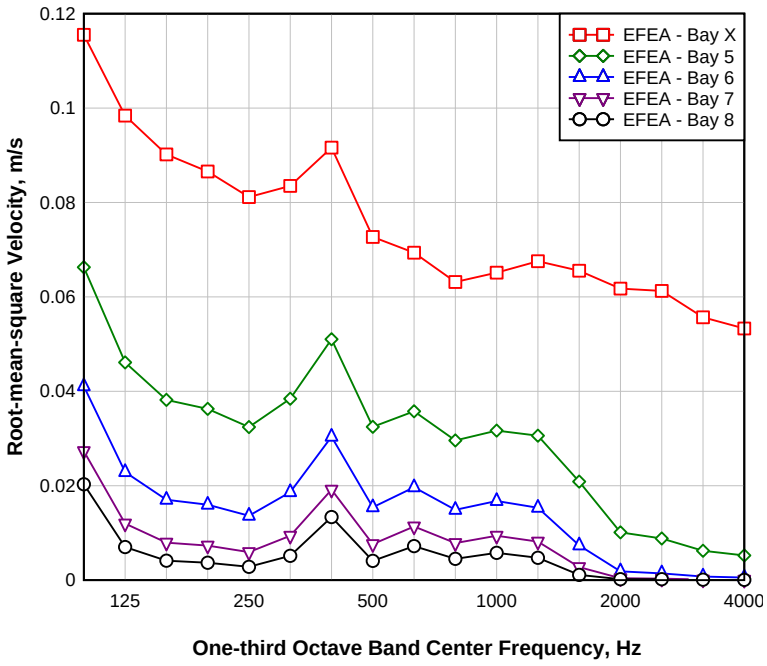

Figure 25. Comet Enflow (EFEA) predicted root-mean-square velocities in the bay subsystems X, 5-8 of the floor-equipped composite cylinder.

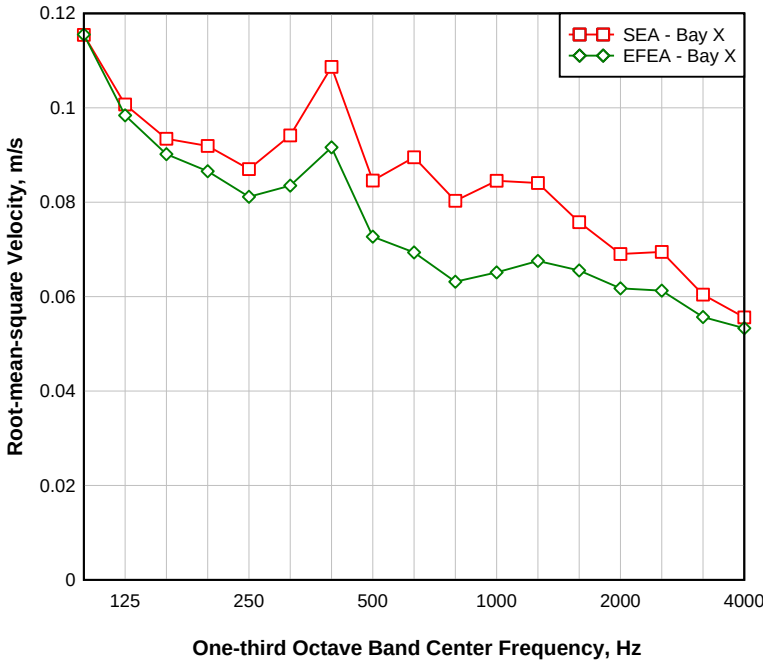

Figure 26. VA One (SEA) and Comet Enflow (EFEA) predicted root-mean-square velocities in the excitation bay subsystem X of the floor-equipped composite cylinder.

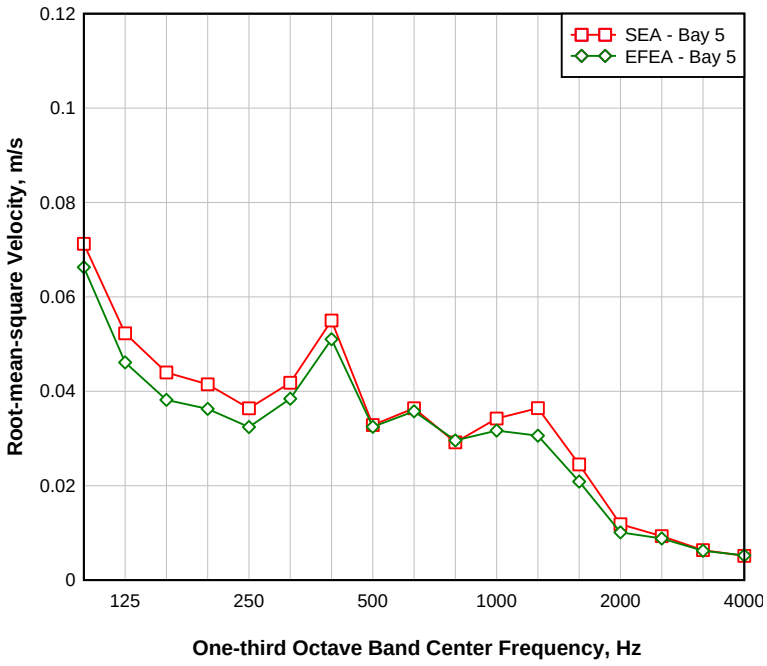

Figure 27. VA One (SEA) and Comet Enflow (EFEA) predicted root-mean-square velocities in the excitation bay subsystem 5 of the floor-equipped composite cylinder.

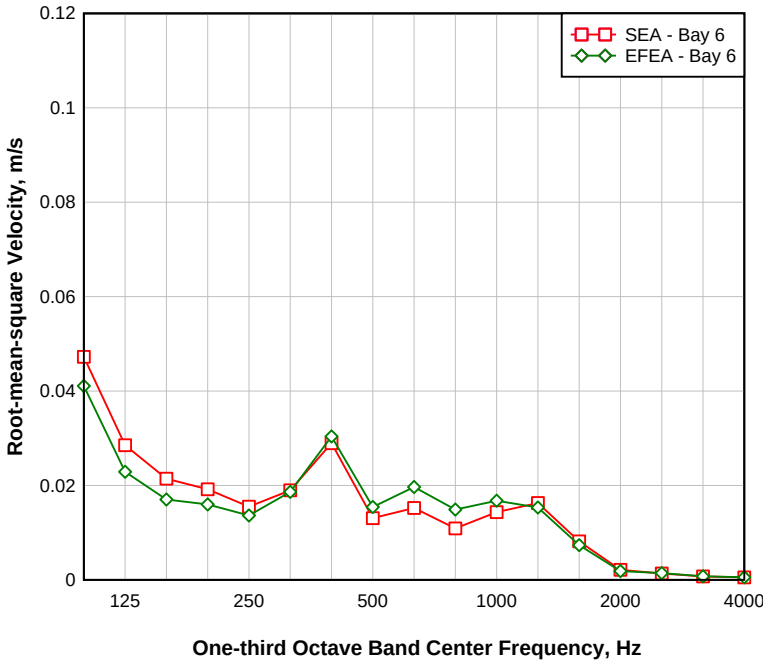

Figure 28. VA One (SEA) and Comet Enflow (EFEA) predicted root-mean-square velocities in the excitation bay subsystem 6 of the floor-equipped composite cylinder.

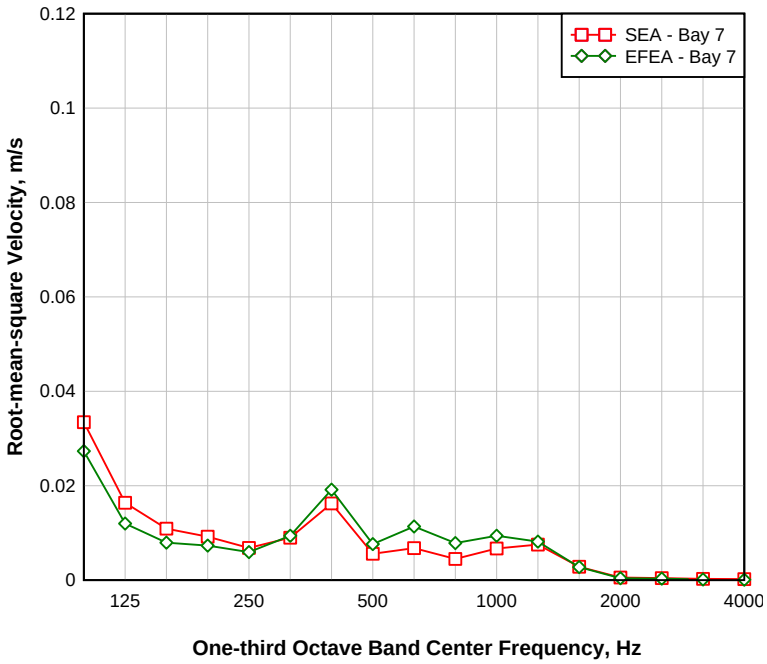

Figure 29. VA One (SEA) and Comet Enflow (EFEA) predicted root-mean-square velocities in the excitation bay subsystem 7 of the floor-equipped composite cylinder.

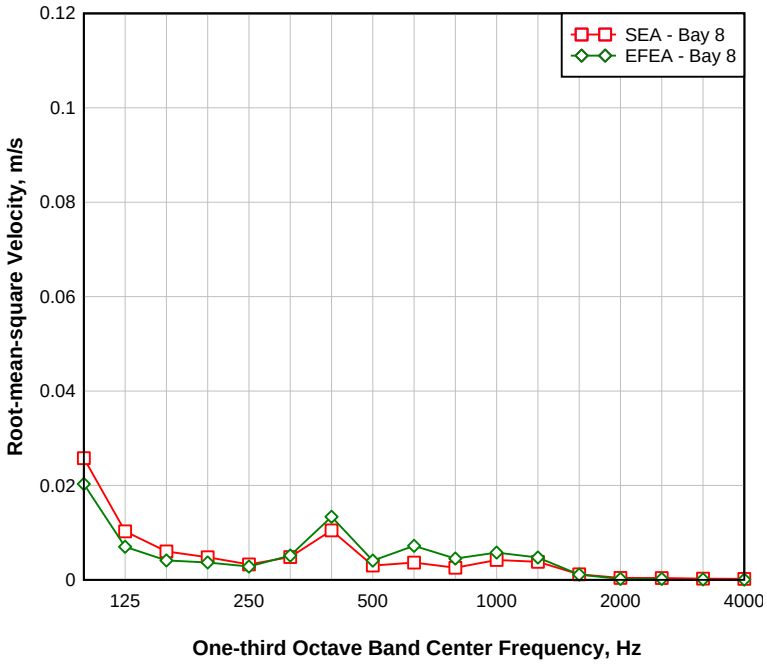

Figure 30. VA One (SEA) and Comet Enflow (EFEA) predicted root-mean-square velocities in the excitation bay subsystem 8 of the floor-equipped composite cylinder.

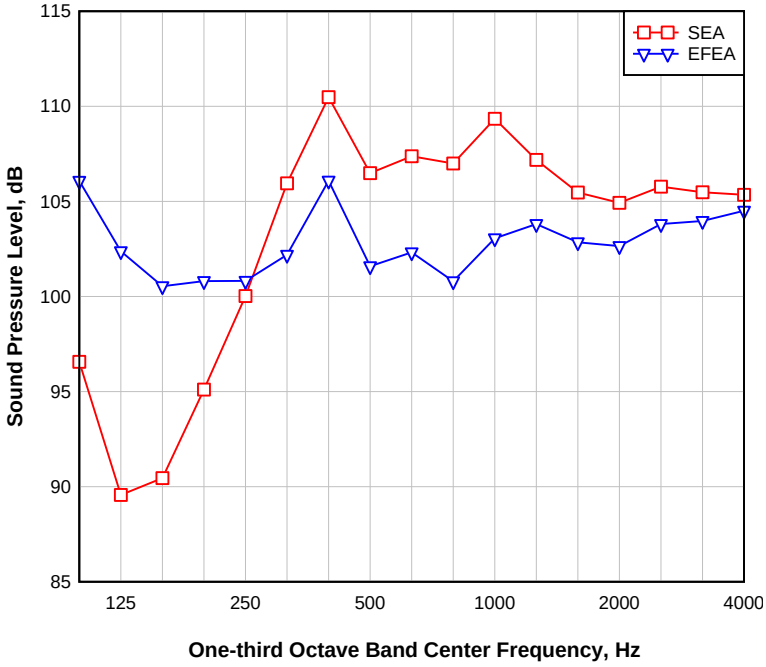

Figure 31. VA One (SEA) and Comet Enflow (EFEA) predicted sound pressure levels in the upper acoustic cavity subsystem of the floor-equipped composite cylinder.

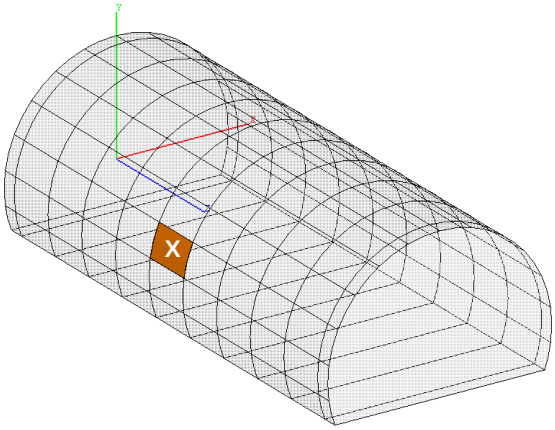

Figure 32. Two subsystem configuration of a bay and an acoustic cavity excited by unit input power on the bay.

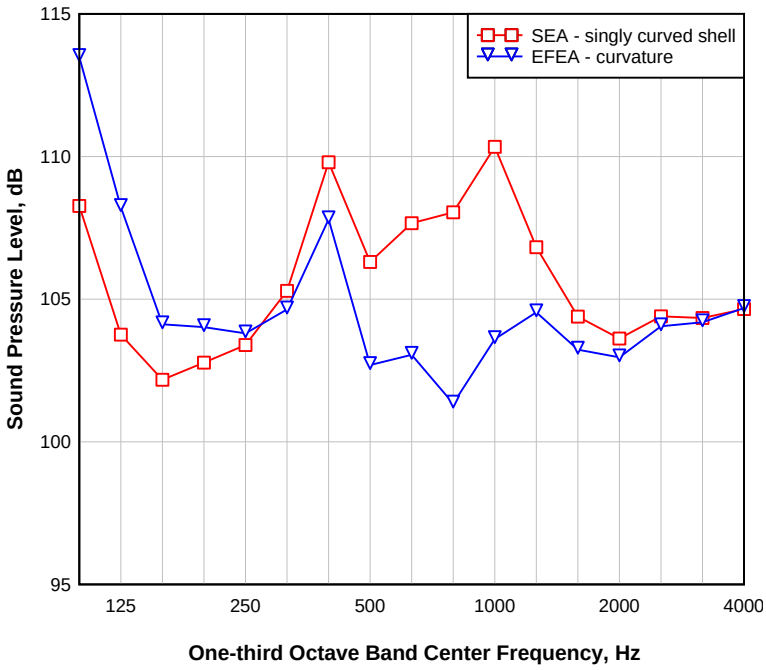

Figure 33. Predicted sound pressure levels in the acoustic cavity for unit power excitation of a singly curved shell (VA One - SEA) or a plate to which curvature was applied (Comet Enflow - EFEA).

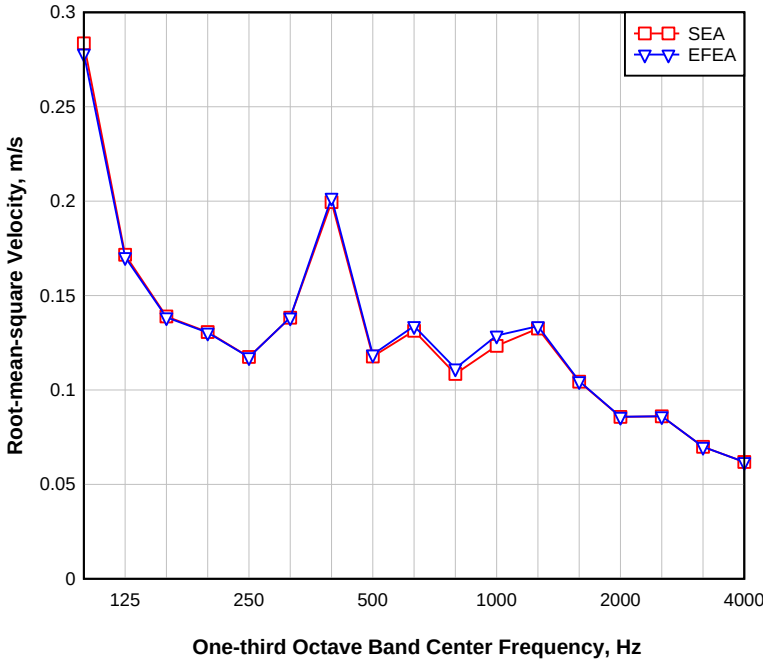

Figure 34. Predicted root-mean-square velocities for unit power excitation of a singly curved shell (VA One - SEA) or a plate element to which curvature was applied (Comet Enflow - EFEA).

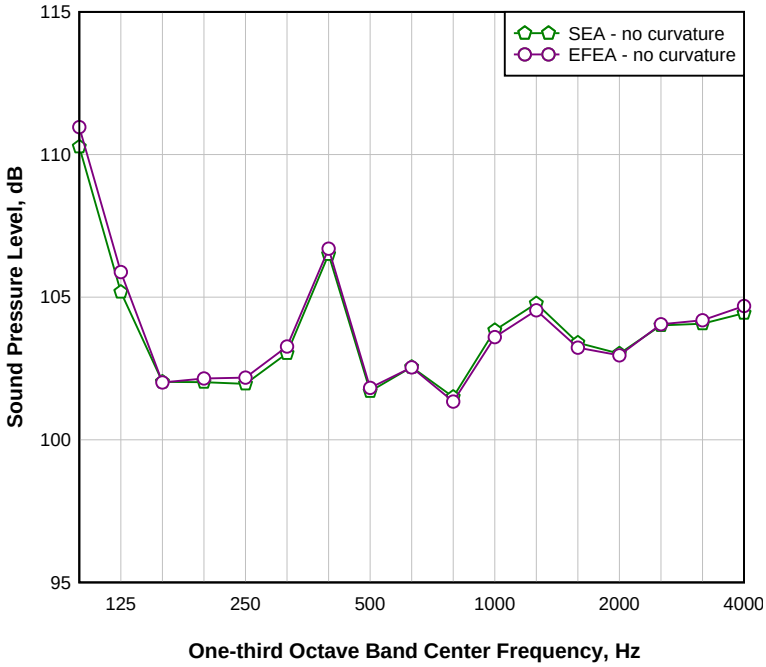

Figure 35. VA One (SEA) and Comet Enflow (EFEA) predicted sound pressure levels in the acoustic cavity for unit power excitation of the flat shell subsystem.

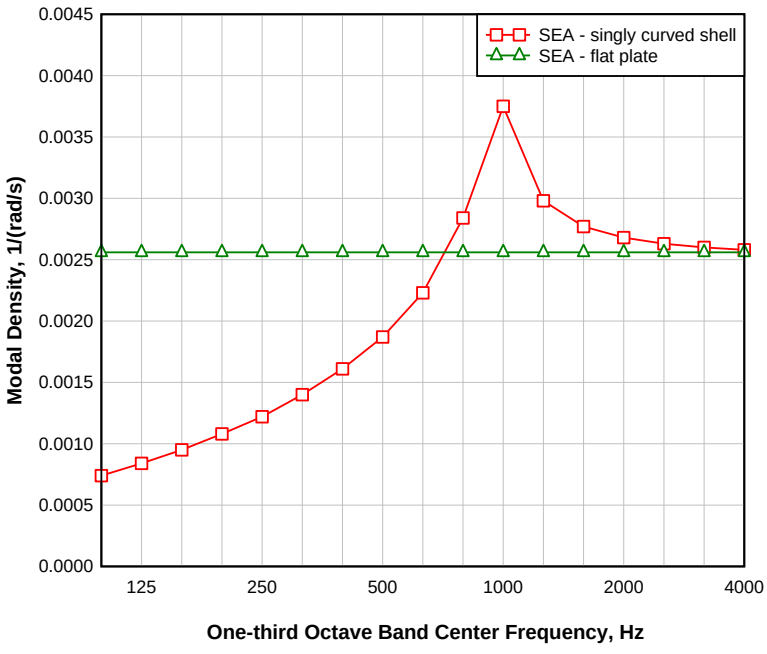

Figure 36. VA One (SEA) predicted modal density for a singly curved orthotropic shell and a flat orthotropic plate.

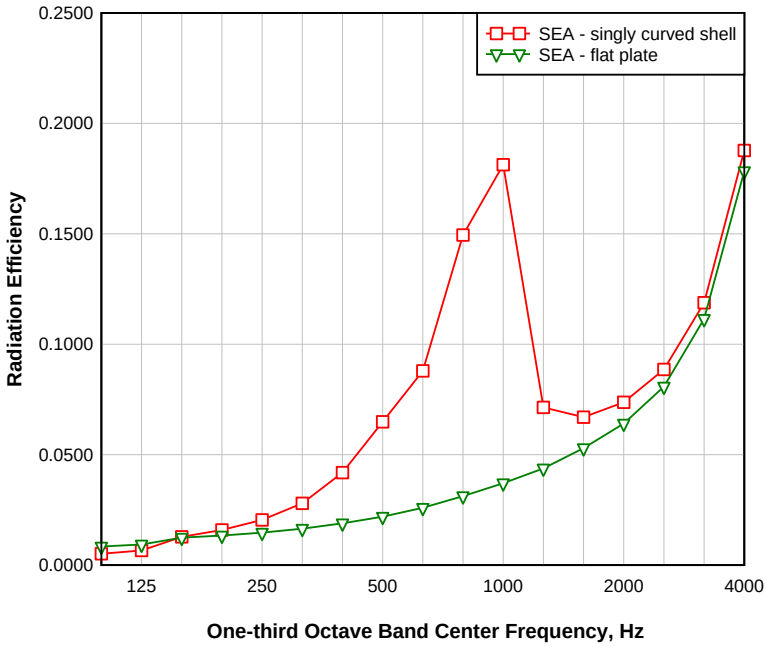

Figure 37. VA One (SEA) predicted radiation efficiency for a singly curved shell and a flat plate.

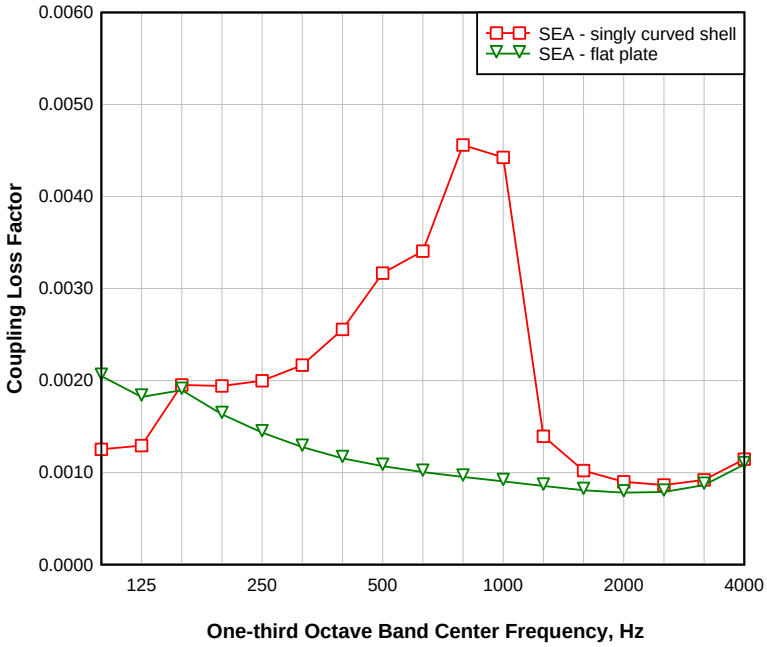

Figure 38. VA One (SEA) predicted coupling loss factor for a singly curved shell or a flat plate connected to the acoustic cavity.

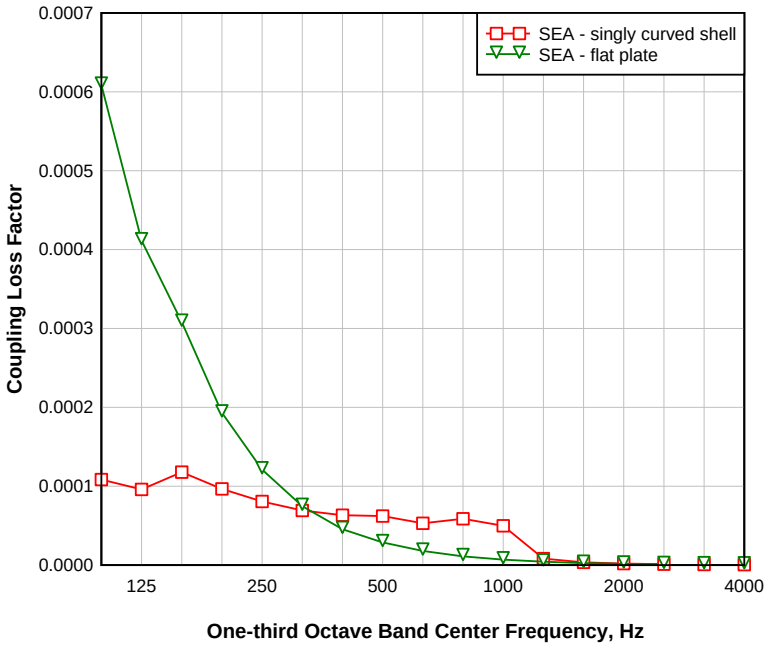

Figure 39. VA One (SEA) predicted coupling loss factor for the acoustic cavity connected to a singly curved shell or a flat plate.

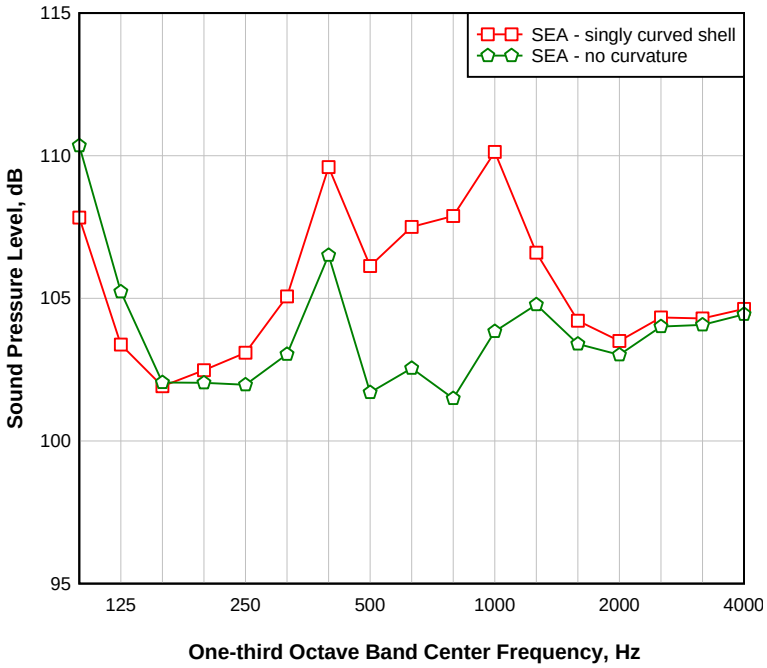

Figure 40. VA One (SEA) predicted sound pressure levels in the acoustic cavity for unit power excitation of the flat or curved shell bay subsystem.

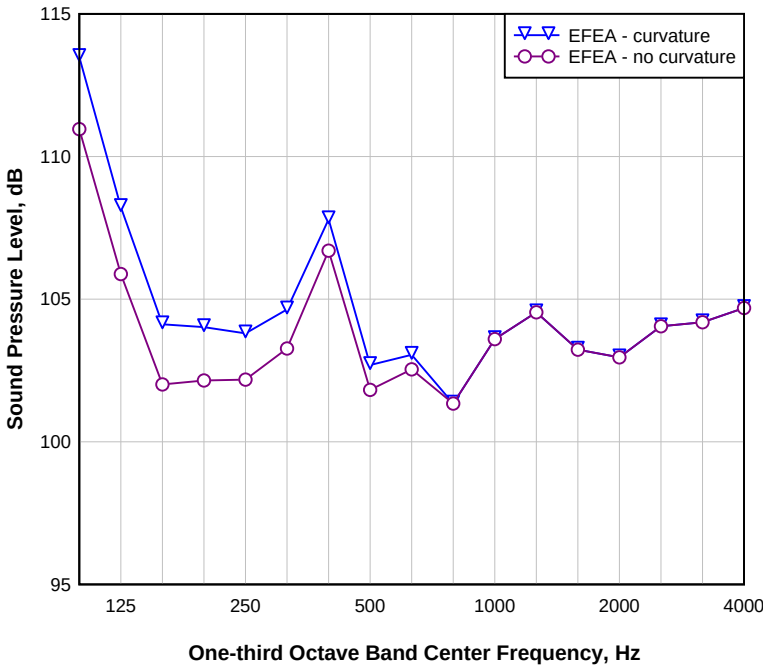

Figure 41. Comet Enflow (EFEA) predicted sound pressure levels in the acoustic cavity for unit power excitation of the flat or curved shell bay subsystem.

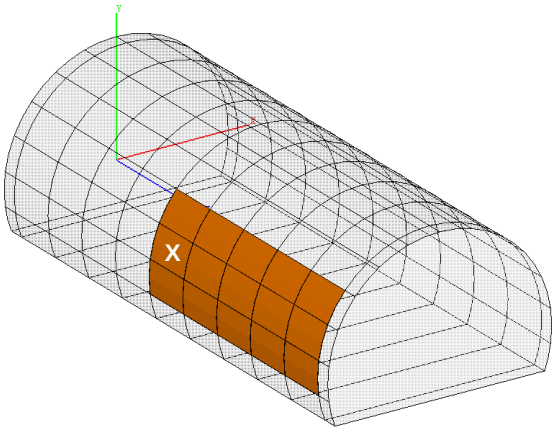

Figure 42. Sidewall structure subsystem (area of fifteen bays; no stiffeners) connected to the acoustic cavity subsystem.

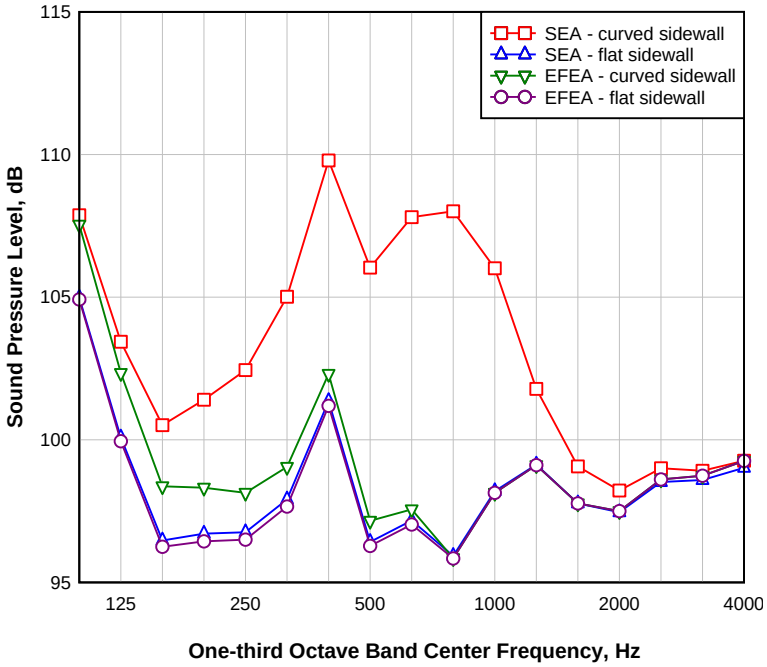

Figure 43. VA One (SEA) and Comet Enflow (EFEA) predicted sound pressure levels in the acoustic cavity for unit power excitation applied to a flat or curved sidewall structure with an area equal to fifteen single bays.

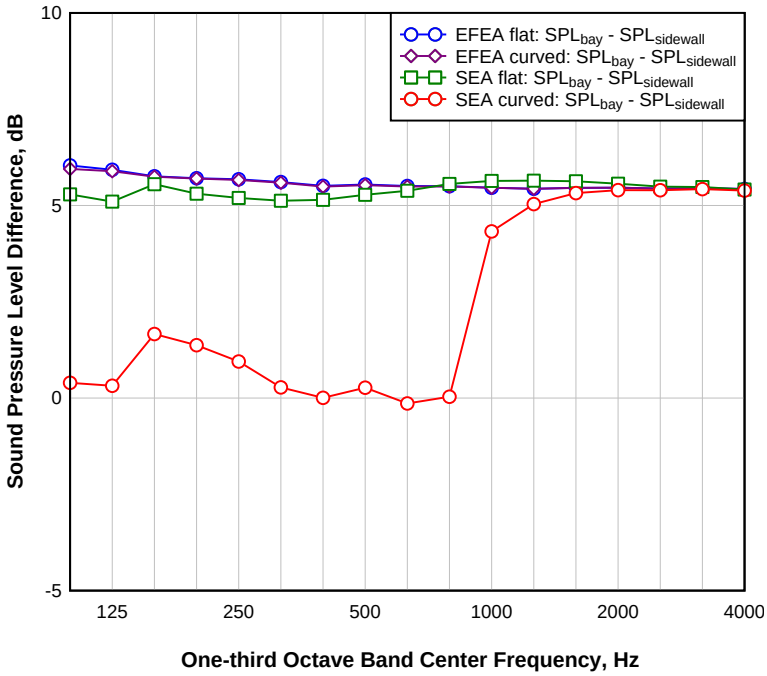

Figure 44. Cavity sound pressure level differences due to unit power excitation of the single bay or the sidewall structure (flat as well as curved) as predicted by VA One (SEA) and Comet Enflow (EFEA).

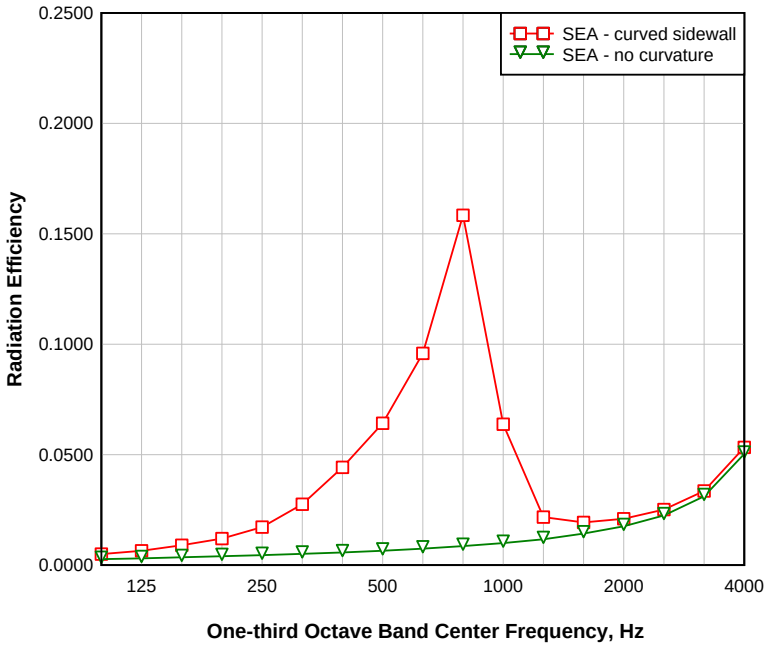

Figure 45. VA One (SEA) predicted radiation efficiency for a flat or curved sidewall structure with a total area equal to fifteen single bays.

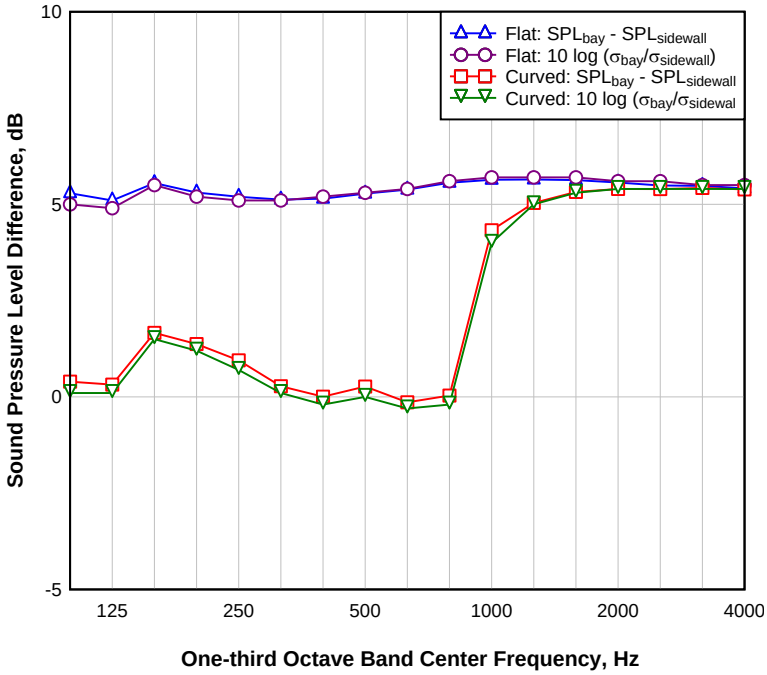

Figure 46. Cavity sound pressure level differences due to unit power excitation of the flat or curved, bay or sidewall structure (fifteen times the bay area) as predicted by VA One (SEA) and compared to 10 $\log(\sigma_{bay}/\sigma_{sidewall})$.

REPORT DOCUMENTATION PAGE

Form Approved
OMB No. 0704-0188

1. REPORT DATE *(DD-MM-YYYY)*	2. REPORT TYPE	3. DATES COVERED *(From - To)*
01- 08 - 2011	Technical Memorandum	

4. TITLE AND SUBTITLE

Statistical Energy Analysis (SEA) and Energy Finite Element Analysis (EFEA) Predictions for a Floor-Equipped Composite Cylinder

5a. CONTRACT NUMBER

5b. GRANT NUMBER

5c. PROGRAM ELEMENT NUMBER

6. AUTHOR(S)

Grosveld, Ferdinand W.; Schiller, Noah, H.; Cabell, Randolph H.

5d. PROJECT NUMBER

5e. TASK NUMBER

5f. WORK UNIT NUMBER

877868.02.07.07.04.01.01

7. PERFORMING ORGANIZATION NAME(S) AND ADDRESS(ES)

NASA Langley Research Center
Hampton, VA 23681-2199

8. PERFORMING ORGANIZATION REPORT NUMBER

L-20035

9. SPONSORING/MONITORING AGENCY NAME(S) AND ADDRESS(ES)

National Aeronautics and Space Administration
Washington, DC 20546-0001

10. SPONSOR/MONITOR'S ACRONYM(S)

NASA

11. SPONSOR/MONITOR'S REPORT NUMBER(S)

NASA/TM-2011-217171

12. DISTRIBUTION/AVAILABILITY STATEMENT

Unclassified Unlimited
Subject Category 71
Availability: NASA CASI (443) 757-5802

13. SUPPLEMENTARY NOTES

14. ABSTRACT

Comet Enflow is a commercially available, high frequency vibroacoustic analysis software founded on Energy Finite Element Analysis (EFEA) and Energy Boundary Element Analysis (EBEA). Energy Finite Element Analysis (EFEA) was validated on a floor-equipped composite cylinder by comparing EFEA vibroacoustic response predictions with Statistical Energy Analysis (SEA) and experimental results. Statistical Energy Analysis (SEA) predictions were made using the commercial software program VA One 2009 from ESI Group. The frequency region of interest for this study covers the one-third octave bands with center frequencies from 100 Hz to 4000 Hz.

15. SUBJECT TERMS

Acoustics; Composite cylinder; Energy finite element analysis; Interior noise; Statistical energy analysis; Vibro-acoustics

16. SECURITY CLASSIFICATION OF:			17. LIMITATION OF ABSTRACT	18. NUMBER OF PAGES	19a. NAME OF RESPONSIBLE PERSON
a. REPORT	b. ABSTRACT	c. THIS PAGE			STI Help Desk (email: help@sti.nasa.gov)
					19b. TELEPHONE NUMBER *(Include area code)*
U	U	U	UU	49	(443) 757-5802